UC Irvine
UC Irvine Previously Published Works

Title

How Do Model Biases Affect Large-Scale Teleconnections That Control Southwest U.S. Precipitation? Part II: Seasonal Models

Permalink

https://escholarship.org/uc/item/6sk408sm

Journal

Journal of Climate, 38(1)

ISSN

0894-8755

Authors

Peings, Y
Dong, C
Magnusdottir, G

Publication Date

2025

DOI

10.1175/jcli-d-24-0287.1

Peer reviewed

How Do Model Biases Affect Large-Scale Teleconnections That Control Southwest U.S. Precipitation? Part II: Seasonal Models

Y. PEINGS,[a] C. DONG,[a] AND G. MAGNUSDOTTIR[a]

[a] *Department of Earth System Science, University of California, Irvine, Irvine, California*

ABSTRACT: We explore the skill in predicting southwest United States (SWUS) October–March precipitation and associated large-scale teleconnections in an ensemble of hindcasts from seasonal prediction systems. We identify key model biases that degrade the models' capability to predict SWUS precipitation. The subtropical jet in the Pacific sector is generally too zonal and elongated. This is reflected in the models' North Pacific ENSO teleconnections that are generally too weak with exaggerated northwest–southeast tilt, compared to observations. Also, the models are too dependent on tropical, El Niño–like, wave train anomalies for producing high seasonal SWUS precipitation, when in observations there is a larger influence of zonal Rossby wave trains such as the one observed in 2016/17. Overall, this is consistent with biases in the basic-flow-inducing errors in the propagation of zonal wave trains in the North Pacific, which affects SWUS precipitation downstream. Although higher skill may be gained from reducing mean flow biases in the models, a case study of the 2016/17 winter illustrates the great challenge behind skillful seasonal prediction of SWUS precipitation. Unsurprisingly, the almost record-breaking precipitation observed that year in the absence of ENSO is not predicted in the hindcasts, and model perturbation experiments suggest that even a perfect prediction of tropical sea surface temperature and tropical atmospheric variability would not have sufficed to produce a reasonable seasonal precipitation prediction. On a more positive note, our perturbation experiments suggest a potential role for Arctic variability that supports findings from prior studies and suggests reexamining high-latitude drivers of SWUS precipitation.

KEYWORDS: Atmospheric circulation; Teleconnections; Rainfall; Seasonal forecasting; General circulation models; Interannual variability

1. Introduction

The western United States is a region where seasonal and long-term prediction of precipitation is critical for managing water resources. Water reservoir depletion during prolonged droughts directly impacts water supply and hydroelectric infrastructures, inducing great stress on society at large. Seasonal prediction is made difficult by the fact that the total rain received in a year mostly comes from short-lived weather systems and associated atmospheric rivers (ARs; Ralph and Dettinger 2011; Mundhenk et al. 2016). Rain and snowfall brought by ARs in winter and spring are then stored in groundwater basins, snowpacks, and reservoirs and provide most of the water resources in the southwest United States (SWUS). The challenge for SWUS precipitation forecasting is to predict how many, and where, ARs will hit the West Coast, since a few AR landfalls can make the difference between a dry year and a water-abundant year (Dettinger 2013). This is especially true over California (CA) where the distribution of precipitation is highly variable between years (e.g., Peings et al. 2022).

The skill of subseasonal and seasonal forecasts in the region is notoriously low (e.g., Sun et al. 2022; Kumar and Chen 2020; Roy et al. 2020; Becker et al. 2022; Jiang et al. 2022) and

insufficient to effectively support water management decisions (Sengupta et al. 2022). Most of the predictability at seasonal time scales comes from slowly evolving components of the climate system, especially sea surface temperature (SST) anomalies associated with El Niño–Southern Oscillation (ENSO), the most prominent mode of climate variability at interannual time scales. ENSO-associated deep convection and latent heat release in the tropical Indo-Pacific drive a Rossby wave response (e.g., Hoskins and Karoly 1981; Trenberth et al. 1998), setting up a north-central Pacific trough–ridge during El Niño–La Niña (Horel and Wallace 1981; Deser et al. 2018). El Niño (La Niña) has generally been associated with a wet (dry) SWUS (Ropelewski and Halpert 1986; L'Heureux et al. 2015), but this teleconnection is intermittent and only explains 25% of interannual SWUS precipitation variability (Lee et al. 2018; Mamalakis et al. 2018; Kumar and Chen 2020; Jiang et al. 2022; Karanja et al. 2023). For example, the 2016 water year (WY; defined as the amount of rainfall received from 1 October 2015 to 30 September 2016) was near average in terms of SWUS precipitation despite a historically strong El Niño, while the following weak La Niña 2017 WY was historically wet (Wang et al. 2017; Peings et al. 2022). Seasonal forecasts were unsuccessful at forecasting both WYs. Empirical techniques with much less complexity have been shown to equal or outperform the skill of dynamical models in predicting SWUS precipitation (Switanek et al. 2020; Gibson et al. 2021; Switanek and Hamill 2022), providing a benchmark for dynamical forecast systems, but they still exhibit limited skill (DeFlorio et al. 2024).

A requirement for skillful seasonal forecasts is predicting the large-scale atmospheric circulation that drives SWUS precipitation during the cool season (October–April), i.e., the persistence of ridging or troughing in the eastern North Pacific (ENP; e.g., Swain 2015; Mundhenk et al. 2016; Seager and Henderson 2016; Teng and Branstator 2017; Guirguis et al. 2019; Gibson et al. 2020), which regulates the frequency and path of winter storms and ARs that bring precipitation to the west coast of North America (e.g., Gibson et al. 2020; Mundhenk et al. 2016; Swain et al. 2017; Teng and Branstator 2017; Payne and Magnusdottir 2016). Since most SWUS seasonal precipitation is independent of ENSO and instead is associated with Rossby wave trains in the North Pacific (Jiang et al. 2022), the outstanding question for seasonal prediction is whether they are predictable. In Peings et al. (2022), we showed that prescribing observed tropical atmospheric variability in an atmospheric model significantly improved the representation of North Pacific atmospheric patterns, at subseasonal-to-seasonal (S2S; between 2 and 8 weeks, approximately) and seasonal time scales, compared to Atmospheric Model Intercomparison Project (AMIP)–type climate simulations [prescribed SST/sea–ice concentration (SIC)]. Dias et al. (2021) also used nudging to estimate the role of tropical forecast errors in the midlatitudes. Although not addressing real-world predictability, these "perfect tropics" experiments indicated that a significant portion of S2S/seasonal midlatitude atmospheric variability is forced by tropical variability and is not necessarily dependent on ENSO. Teleconnection patterns originating from the tropics must therefore be accurately represented in the models, which requires both a realistic atmospheric basic state and realistic tropical convective forcing (e.g., Hoskins and Ambrizzi 1993; Li et al. 2020; Wang et al. 2020). However, model biases develop quickly after initialization in both S2S and seasonal forecast models, affecting teleconnections associated with ENSO or the Madden–Julian oscillation (MJO) (Bayr et al. 2019; Ma et al. 2021; Garfinkel et al. 2022; Beverley et al. 2023; Williams et al. 2023). There is even evidence that initialization does not bring significant value to the skill of seasonal forecast models, since similar skill for some fields/regions can be obtained through analog forecast techniques using long control runs from the same models (Ding et al. 2018, 2019, 2020).

This work is an extension of Dong et al. (2024; referred to as D24 hereafter), which aimed to reveal model biases that affect subseasonal teleconnections of interest for SWUS precipitation, using an ensemble of S2S hindcasts. We follow the same approach in the present study, but instead we analyze an ensemble of hindcasts from seasonal forecast models. Like D24, the focus is on the cold season [October–March (ONDJFM)], but here we explore the skill and model biases of the forecast systems in terms of both monthly (1 month lead time, month 1) and extended season prediction (ONDJFM seasonal average prediction or months 1–6; see section 2a). Our objective is similar to D24, i.e., highlighting how model biases, in particular in the background flow in the North Pacific, can affect how the models represent tropical–extratropical teleconnections and more generally wave propagation in the midlatitudes. We also use perturbation experiments that were specifically designed to explore

potential predictability in the midlatitude atmospheric variability, extending to the work we presented in Peings et al. (2022). After describing the data and methods in section 2, section 3 describes the results from our different analyses, and section 4 concludes by summarizing and discussing the implications of the results and how they relate to D24.

2. Data and methods

a. Seasonal forecast ensemble

To evaluate seasonal forecasts from dynamical models, we use hindcasts (also called reforecasts) from eight seasonal forecast systems contributing to the Copernicus Climate Change Service (C3S) seasonal forecasts: Centro Euro-Mediterraneo sui Cambiamenti Climatici (CMCC; Gualdi et al. 2020), Deutscher Wetterdienst (DWD; Fröhlich et al. 2021), European Centre for Medium-Range Weather Forecasts (ECMWF; Johnson et al. 2019), Environment and Climate Change Canada (ECCC; Lin et al. 2020), Japan Meteorological Agency (JMA; Yonehara et al. 2020), Météo-France (Batté et al. 2021), the National Centers for Environmental Prediction (NCEP[1]), and the United Kingdom Meteorological Office (UKMO; MacLachlan et al. 2015).

The hindcasts do not cover the same period, with ECMWF having the longest period (1981–2016) and all models providing hindcasts for at least 1993–2016. Only DWD, ECCC, and Météo-France go beyond 2016. When comparing the hindcasts, we mostly use the 1993–2016 period of overlap. The fields analyzed in this study are monthly outputs of precipitation P, SST, mean sea level pressure (SLP), zonal wind at 200 hPa (U200), meridional wind at 200 hPa (V200), and geopotential height at 200 hPa (Z200; referred to as Z200x when the zonal mean is removed), at different lead times. Lead time defines how far from initialization a forecast is, in months. For example, for a forecast initialized in September or on 1 October, predicting October corresponds to a lead time of 1, and month 1 of the forecast is October. Predicting November from the same forecast would then correspond to a lead time of 2, with November being month 2 of the forecast. Predicting the ONDJFM average also corresponds to a lead time of 1 (the target season starts 1 month after initialization), with ONDJFM corresponding to months 1–6 of the forecast.

In the study, we examine two prediction windows:

- **Month 1 or monthly prediction**: It measures the skill of monthly prediction inside the ONDJFM season. For this, for each ONDJFM season, we average the October–March months that correspond to lead time 1 in the different hindcasts initialized between September and March. Each month inside a season then comes from a different hindcast, and it is always month 1 from its hindcast. In other words, *the "month 1" forecast window is the average of October–March monthly forecasts*. Note that because the forecast centers have different protocols when producing

---

[1] https://www.emc.ncep.noaa.gov/emc/pages/numerical_forecast_systems/gfs/documentation_spectralgfs.php.

TABLE 1. Description of the seasonal hindcasts.

Forecast system	Ensemble size	Period and start dates
CMCC-SPS3	40	1993–2016 first of month
DWD-GCFS2.1	30	1993–2019 first of month
ECCC-GEM5.2-NEMO	10	1993–2020 first of month
ECMWF-SEAS5	25	1981–2016 first of month
JMA-CPS3	10	1993–2016 two start dates lagged by 15 days, previous month
Météo-France System 8	25	1993–2018 two last Thursdays of previous month + first of month
NCEP-CFSv2	24	1993–2016 every 5 days, every 6 h, previous month
UKMO-GloSea6	28	1993–2016 1st, 9th, 17th, and 25th of previous month

the hindcasts, lead 1 does not always correspond to the same exact 1-month lead time. As listed in Table 1, some forecast systems/ensemble members are initialized on the first of month 1, while others are initialized in the previous month before lead 1 or during month 0. As an example, for both hindcasts initialized in September (month 0) and/or 1 October, month 1 is October.

• **Months 1–6 or extended season prediction**: It measures the skill for predicting the average ONDJFM seasonal anomalies, on 1 October to the latest. For this, we only use hindcasts initialized in September or 1 October, which for a prediction of the ONDJFM average corresponds to a lead time of 1, but looking into months 1–6 of the hindcast. Unlike the month 1 prediction window, here all months included in an ONDJFM season come from the same hindcast, and *the "month 1–6" forecast window is the forecast of the ONDJFM average*. Seasonal outlooks are typically produced for 3-month averages, but we analyze the extended ONDJFM 6-month season in this paper because this is a forecast window of interest for the SWUS water agencies and other stakeholders (how much precipitation will hit our state this cold season?). Similar analyses for October–December (OND) and January–March (JFM) separately have been done that generally support the main findings of this study. However, each 3-month season has its own characteristics that are not addressed in the present paper and are left for future studies.

Although the protocol for initialization differs among forecast systems, the hindcasts are generally initialized using atmospheric, oceanic, and land surface fields from various reanalyses. The ensemble generation strategies also vary across forecast centers, using a combination of atmospheric, oceanic, and land surface perturbations, as well as stochastic physical perturbations, to generate ensembles of hindcasts of various sizes (Table 1; ensemble sizes vary from 10 to 40). More details on the models, protocols, and initialization techniques can be found in the C3S seasonal multisystem documentation.[2] Because the model outputs and observations have different horizontal and vertical resolutions, they are all interpolated onto a 1° grid for comparison. The ensemble of hindcasts from each model is averaged together to measure one model's performance in prediction. The multimodel performance is measured using the average of each model's

ensemble, such that the same weight is given to each model, regardless of the number of ensemble members they include. When exploring teleconnections associated with ENSO or SWUS precipitation, we concatenate individual ensemble members together rather than using the hindcast ensemble mean. This is motivated by our main research question, i.e., finding model biases that may hamper the representation of these teleconnections. Using individual members concatenated together as one long model run allows us to examine total, rather than forced, variability in the models, and it also greatly increases the sample size (when computing regressions, for example), which increases the robustness of the results.

b. Observational data, indices, and diagnostics

We evaluate model performance by comparing it to reanalysis data from the fifth major global reanalysis produced by ECMWF (ERA5; Hersbach et al. 2020), which uses a data assimilation system to constrain observations from 1940 to the present with a horizontal spatial resolution of 31 km and 137 vertical levels. In addition to ERA5, we use the Hadley Centre Sea Ice and SST dataset (HadISST; Rayner et al. 2003), the Global Precipitation Climatology Project (GPCP, version 2.3) precipitation dataset (Adler et al. 2018), and the Climate Prediction Center (CPC) precipitation dataset, a gauge-based unified precipitation product over the continental United States with a resolution of 0.25° (Chen et al. 2008). CPC is used to examine western U.S. precipitation over the 1948–2023 period, while GPCP is used when precipitation in the Indo-Pacific basin is investigated (1979–2023 period).

An index of seasonal SWUS precipitation is defined as the average ONDJFM precipitation in the domain (236°, 251°E; 31°, 42°N) (see Fig. 1a), over land only, for both observations and the models. CPC data are used for observations. The influence of ENSO on SWUS rainfall is assessed using the Niño-3 index (150°, 90°W; 5°S, 5°N). The Niño-1 + 2 index has a higher correlation with California and SWUS rainfall than the other Niño indices in observations (Jiang et al. 2022). Over 1948–2023, the correlation between our observed ONDJFM SWUS precipitation index and the Niño-1 + 2 index is 0.43. The correlation is 0.37 with the Niño-3 index and 0.33 with the Niño-3.4 index. We choose to perform the analyses with the Niño-3 index because it is more commonly used than the Niño-1 + 2 index, and it has a greater correlation with SWUS precipitation than the Niño-3.4 index. The propagation of Rossby waves is examined using a stationary wavenumber diagnostic (based on the U200 basic state) and

---

[2] https://confluence.ecmwf.int/display/CKB/Description+of+the+C3S+seasonal+multi-system.
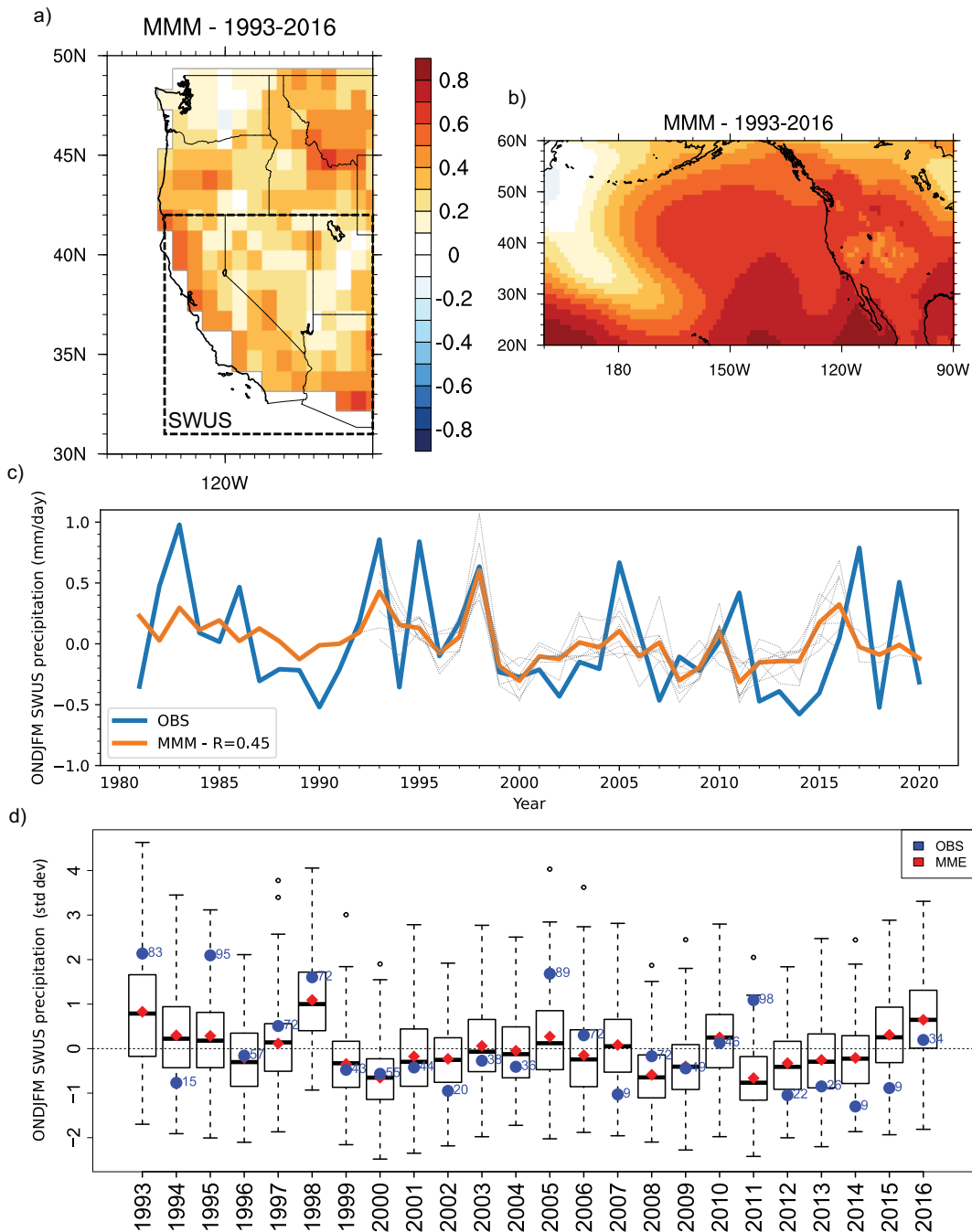
FIG. 1. (a) Skill of the multimodel C3S ensemble over 1993–2016, as measured as the gridpoint correlations between the observed (CPC) and predicted ONDJFM precipitation (multimodel average prediction), from seasonal forecasts initialized in October (or September). (b) As in (a), but for the mean SLP in the North Pacific–North America domain (ERA5 for observations). (c) Time series of the SWUS ONDJFM precipitation index over 1981–2020, from the CPC observations (blue) and the multimodel mean of the C3S seasonal forecasts (orange). Individual model ensemble means are shown with dotted gray lines, which span different periods. The correlation between the observed SWUS index and the prediction from the multimodel ensemble mean is 0.45 over the whole 1981–2020 period (with only ECMWF over 1981–92), 0.52 over 1993–2016 (all the models), and 0.43 over 1993–2016 after the 1998 year is removed. (d) Ensemble distribution of the predicted SWUS ONDJFM precipitation index, based on the 192 ensemble members from the eight model hindcasts, for each year 1993–2016. The boxplots indicate the median and upper and lower quartiles of the distribution. The whiskers indicate the minimum and maximum values, and the circles are outliers. The ensemble mean is marked by a red diamond, and the corresponding observed value is marked by a blue circle, with its percentile rank relative to the model spread in blue text.

ray tracing, similar to part I of this study (D24). To avoid replication of the description of these diagnostics, we refer the reader to D24 for details on the methodology.

We characterize the presence of a strong seasonal zonal wave train in the North Pacific using an index we call the North Pacific waviness index. The index is computed using ONDJFM V200 anomalies (calculated from respective climatologies for observations, seasonal models, and perturbation experiments). We choose V200 because upper-level meridional wind emphasizes the presence of zonal wave trains in the atmosphere, as an alternation of positive and negative anomalies around the trough–ridges that constitute the wave train. For each season, we calculate the zonal gradient of the V200 anomalies, which measures meanders in the flow. Then, we calculate its absolute value, and the resulting field is spatially averaged (with area weights) in a large North Pacific domain (140°, 240°E; 35°, 65°N). The index is then normalized according to its own climatology/standard deviation. The greater the index, the greater the absolute magnitude of gradients in the V200 anomalies, i.e., the greater waviness in the zonal flow.

c. Perturbation experiments for the 2017 case study

Perturbation experiments have been designed to examine the unexpectedly wet WY 2017 over CA/SWUS. Following the methods described in Peings et al. (2022), we use the Whole Atmosphere Community Climate Model, version 4 (WACCM4; Marsh et al. 2013), to perform a set of seasonal experiments that include a hierarchy of forcing for ONDJFM 2017. WACCM4 has a horizontal resolution of 1.9° latitude by 2.5° longitude, and it is a high-top model with 66 vertical levels up to 5.1×10^{-6} hPa (~140 km). We use the specified chemistry version of WACCM4 (SC-WACCM4; Smith et al. 2014), which is computationally less expensive to run but simulates dynamical stratosphere–troposphere coupling and stratospheric variability that are comparable to the interactive chemistry model version.

The simulations follow the AMIP experimental design; i.e., the AGCM is constrained by observed SST and SIC. Monthly SST/SIC from the merged Hadley/NOAA-OI dataset (Hurrell et al. 2008) is prescribed to the atmosphere, with a linear interpolation to derive daily SST/SIC from the monthly values and ensure a smooth evolution of SST/SIC. External forcings (greenhouse gasses, aerosols, volcanoes, ozone, and solar radiation) follow their historical 1978–2017 values (Meinshausen et al. 2011). Since WACCM4 does not simulate the QBO, we use the QBO prescription that is an option feature of WACCM. The QBO is prescribed through nudging of the equatorial stratospheric winds to observed radiosonde data, between 22°S and 22°N, and from 86 to 4 hPa. The following set of experiments has been performed:

- **AMIP:** Our control experiment consists of an ensemble of 10 AMIP runs, covering the 1978–2016 period, that are forced with observed 1978–2016 SST/SIC. It is used as a baseline to estimate the climatology of our model when analyzing the atmospheric response in the perturbation experiments.

- **AMIP17:** The first perturbation experiment consists of 100 ensemble members for the ONDJFM 2016/17 season that are forced with observed 2016/17 SST/SIC. The ensemble members are branched from the 1 October 2016 initial conditions from AMIP, and a large ensemble is created by adding tiny temperature perturbations in the initial conditions (Kay et al. 2015).

- **AMIP-TROP17**: This experiment is similar to AMIP17, but it includes nudging of tropical variability to impose the observed 2016/17 tropical variability in the model and examine the response in the midlatitudes. The method is described in detail in Peings et al. (2022). Temperature, wind, and surface pressure are relaxed toward 3-h variability from the MERRA-2 reanalysis (Gelaro et al. 2017) in the tropical troposphere (22°S–22°N, from the surface up to 150 hPa). This experiment consists of 100 ensemble members.

- **AMIP-TRHL17**: This experiment is similar to AMIP-TROP17, but it also includes nudging of Arctic variability (north of 60°N, up to 300 hPa) to examine the potential influence of high-latitude variability on observed anomalies in the midlatitudes. We also discuss an additional experiment, AMIP-HL17, that includes nudging of Arctic variability alone (no tropical nudging). It also includes 100 ensemble members.

This set of experiments allows us to estimate the role of global SST, tropical variability, and high-latitude variability, in one of the wettest years on record in CA that occurred under weak La Niña conditions.

3. Results

a. Skill of the seasonal forecast ensemble

As mentioned in the introduction, the skill of seasonal forecasts for SWUS/California precipitation is low (e.g., Kumar and Chen 2020). We start by assessing the skill of our ensemble of models for western U.S. seasonal precipitation, with individual model skill shown in Fig. S1 in the online supplemental material. Figure 1a shows the skill of the C3S models in predicting ONDJFM precipitation over the western United States. This is shown as a gridpoint correlation between observed ONDJFM mean precipitation and the prediction from the multimodel ensemble mean (average of model ensemble means) for the 1993–2016 period that includes all models. Although mostly positive correlations are found across the western United States, generally the correlations are under 0.6, i.e., less than 35% of the explained variance. This skill remains too low for real-world application by users such as water managers and other stakeholders.

Figure 1b shows that higher skill is obtained in predicting the seasonal-mean large-scale atmospheric circulation, through gridpoint correlations of the ONDJFM mean sea level pressure in the ensemble prediction versus observations (ERA5 reanalysis), but the correlations are only about 0.6, once again only 35% of the explained variance in seasonal sea level pressure variability in the region. The multimodel ensemble prediction of the ONDJFM SWUS precipitation index has a correlation of 0.45 with observations over 1981–2020

TABLE 2. Correlation coefficient between each model's predicted SWUS P index and observations, over 1993–2016. For models that include a longer time period, the correlation coefficient over the full period is given in parentheses.

Model	MMM	CMCC	DWD	ECCC	ECMWF	JMA	Météo -France	NCEP	UKMO
Skill (R)	0.52 (0.45)	0.53	0.38 (0.34)	0.5 (0.42)	0.49 (0.46)	0.47	0.65 (0.64)	0.23	0.41

(Fig. 1c; ECMWF only over 1981–92). Over the 1993–2016 period that includes all models, the correlation is 0.52. Individual model correlations are given in Table 2. One of the best ensemble mean predictions is found for WY 1998, a notoriously successful El Niño year for seasonal forecasting (Barnston et al. 1999). The ensemble prediction is close to the observed value with a small spread among the ensemble members (i.e., good confidence in the forecast). After removing 1998, the correlation drops to 0.43 or only 20% of the explained variance in the index. The seasonal prediction system is not able to capture other extreme years, such as the very wet year of 2017 or the very dry year of 2014 (Fig. 1c). This is problematic for real-world applicability of the forecasts since extreme water years are the ones that matter for water management and decision-making. Some individual models exhibit higher skill than the multimodel mean in certain regions, for example, Météo-France in Northern California (Fig. S1f) and in general over the SWUS (Table 2), but as we will see later, Météo-France is one of the most biased models when it comes to the North Pacific mean atmospheric circulation and teleconnections. It is therefore difficult to attribute better skill in this model to a better representation of important processes for SWUS precipitation, and we need to remember that the sampling size is too small to address the skill of a model with high confidence. Figure S2 shows a similar time series as Fig. 1c but for OND and JFM (months 1–3 for both). Higher skill is achieved in JFM ($R = 0.63$) versus OND ($R = 0.35$), as expected from more defined large-scale atmospheric circulation patterns and teleconnections in JFM compared to OND. In this regard, the skill we show for ONDJFM is representative of a middle ground between the two forecast seasons.

It is important to remember that for each hindcast year, we compare a single realization of observed variability to a single model, or multimodel, ensemble mean. When the ensemble mean misses an observed anomaly, the observed value may still fall within the spread of the ensembles, i.e., within expectations from internal variability (Chen and Kumar 2018). This is illustrated in Fig. 1d, which compares the observed value of the SWUS precipitation index to the distribution of all individual ensemble members from the model hindcasts, for each year 1993–2016. The percentile rank of the observed value is given for each year, and we can verify that for every one of these years, the observed precipitation anomaly falls within the distribution of model predictions (192 ensemble members in total).

Before examining the drivers of SWUS seasonal precipitation, we analyze how precipitation is represented in the models. A composite of high SWUS precipitation in observations is shown in Fig. 2a. This is an average of ONDJFM precipitation anomalies for seasons with above one standard deviation of the ONDJFM SWUS index (15 years of the 1948–2023

period, CPC data). For this analysis, we use the full available datasets for observations and the models rather than comparing them over the 1993–2016 period of overlap. This increases the sample size for the observed composite on the SWUS precipitation index. For each model, we use all ensemble members concatenated together and not the ensemble mean. The multimodel mean is then the average of each model's composite. The potential influence from low-frequency modes of variability may affect analyses when comparing different time periods, but because the SWUS precipitation index exhibits little low-frequency variability over 1948–2023, this does not have a major influence here.

Anomalously high precipitation is found over most of California, with little precipitation in the inland desert regions, showing that our SWUS index mostly represents CA precipitation, the region most affected by October–March atmospheric rivers from the North Pacific. Figure 2b shows the multimodel mean bias as a difference from Fig. 2a for month 1, while Fig. 2c shows the bias for months 1–6. The bias in high SWUS seasonal precipitation anomaly varies only slightly with lead time, mostly representing a slight overestimation of precipitation over central California. However, this only shows the mean bias and not differences in the distribution of seasonal precipitation. To examine the latter, Fig. 2d shows the observed distribution of the ONDJFM SWUS P index in observations (blue) and in all the hindcasts from the multimodel ensemble (orange) for month 1. As can be seen from the difference in distribution, the models tend to underestimate the precipitation deficit during dry seasons, while overestimating extreme precipitation years relative to observations. This results in a flatter distribution than in observations, and on average, it corresponds to a slight overestimation in climatological SWUS seasonal precipitation (Fig. 2b). For months 1–6 (ONDJFM average) that is the focus of this study, the same bias in the distribution is slightly amplified, with even less frequent dry seasons and more frequent and extreme wet seasons.

b. Representation of the basic atmospheric state and ENSO teleconnection in the North Pacific

In this section, we begin with evaluating how the seasonal forecast models represent the atmospheric basic state and SST in the North Pacific, during our ONDJFM season of interest and over the overlapping 1993–2016 period, for a direct comparison with observations and among models. All analyses use ONDJFM seasonal averages. As explained in section 2a, the hindcast ensemble members are concatenated together for the regression analyses, which yields a sample size of at least 240 ONDJFM seasons for the models with 10 ensemble members, up to 960 for CMCC and its 40 ensemble members. This is of course significantly larger than observations for which
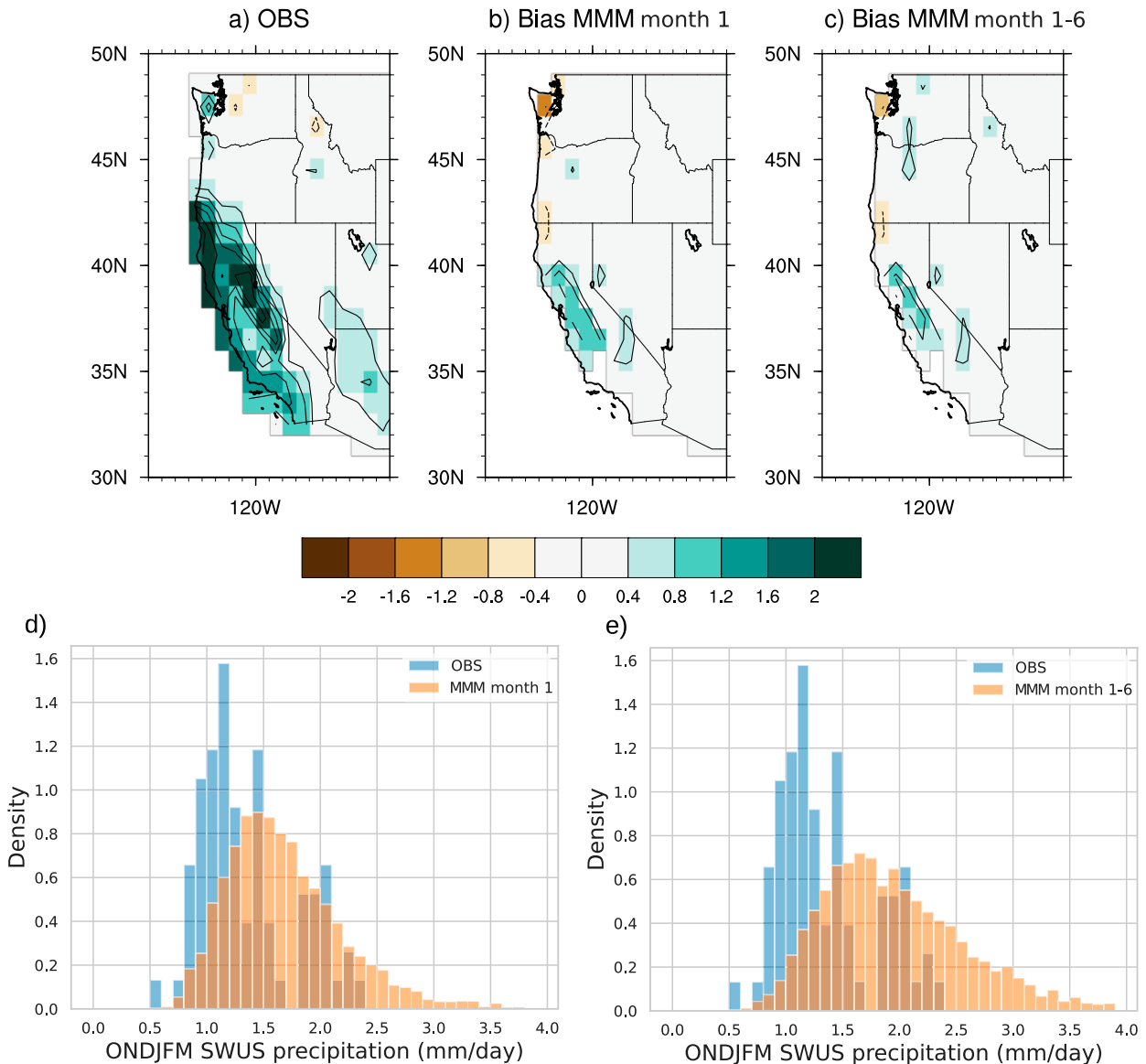
FIG. 2. (a) Composite of precipitation (mm day^{-1}) on the high ONDJFM SWUS precipitation index (+1 standard deviation) in the CPC observations (1948–2023). (b) Bias of the same quantity in the multimodel ensemble, for month 1. (c) As in (b), but for months 1–6. (d) Histogram of the ONDJFM SWUS precipitation index (mm day^{-1}), in observations (CPC, 1948–2023) and in the ensemble of C3S models, for month 1 (5088 seasons). (e) As in (d), but for months 1–6.

assessment of the teleconnection patterns is less robust than for the models. Figure 3a shows the observed climatology of SST and U200. Figures 3b and 3c illustrate the ENSO teleconnection in observations, as a regression of SST and U200 (Fig. 3b), and P and Z200x (Fig. 3c), on the Niño-3 index. Z200x is the 200-hPa geopotential height after removing its zonal mean, which highlights large-scale stationary waves. We then examine how the models represent each of these quantities by plotting the multimodel mean bias (deviation from observations) for month 1 (Figs. 3d–f) and for months 1–6 (Figs. 3g–i).

An important climate feature for seasonal prediction in the SWUS is the East Asian jet stream (EAJS), the most intense

subtropical jet on Earth, easily identifiable in Fig. 3a (black contours). The EAJS, acting as a waveguide for Rossby waves generated in the tropics and in higher latitudes, must be accurately represented in climate models to simulate realistic tropics–extratropics teleconnections as well as zonal wave propagation over the North Pacific (Trenberth et al. 1998; Zhang and Villarini 2018). As can be seen in Figs. 3d and 3g, the multimodel ensemble exhibits a bias in the EAJS, whereby too-strong U200 anomalies are simulated to the southeast of the jet core. This bias represents a too-zonally elongated jet in the central Pacific. The bias increases with lead time, resulting in a more pronounced bias in the month 1–6 predictions (Fig. 3g).
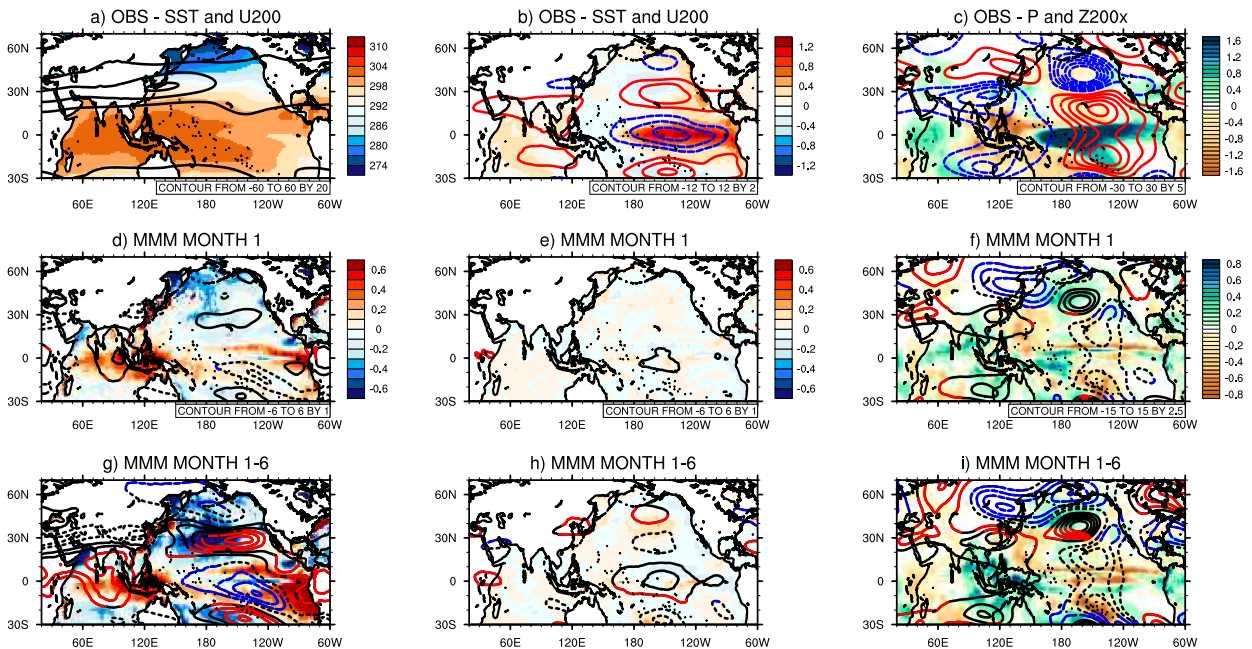
FIG. 3. (a) Observed climatology (1993–2016) of ONDJFM SST (HadISST, shading, 3°C interval) and ONDJFM U200 (ERA5, contours, 20 m s^{-1} contour interval). (b) ENSO teleconnection in observations (1993–2016), as the regression of ONDJFM SST (HadISST, shading, 0.2°C interval) and of ONDJFM U200 (ERA5, contours, 2 m s^{-1} contour interval) on the ONDJFM Niño-3 index. For U200, positive (negative) contours are in red (blue). (c) Regression of ONDJFM precipitation (GPCP, shading, 0.2 mm day^{-1} interval) and of ONDJFM Z200x (ERA5, contours, 5-m contour interval) on the ONDJFM Niño-3 index. For Z200x, positive (negative) contours are in red (blue). (d)–(f) Corresponding bias for month 1 in the C3S seasonal models, as the difference between the multimodel average and observations. Anomalies that are greater than 50% of the observed climatology are in color (red for positive and blue for negative values). In (d), the contour interval for U200 is 1 m s^{-1}. In (e) and (f), the contour intervals are half the values of (b) and (c), i.e., 1 m s^{-1} for U200 and 2.5 m for Z200x. (g)–(i) As in (d)–(f), but for months 1–6.

The jet being too zonal and elongated in the subtropical North Pacific is associated with too-warm SST in the eastern tropical Pacific and the Maritime Continent region (shading in Figs. 3d,g). As shown in Fig. S3, this multimodel mean view hides disparities among models. Most models simulate a too-zonal and elongated EAJS with varying amplitude for the bias, except for ECMWF and JMA. The bias in SST also varies greatly with models, being generally too warm in the tropical Pacific and Indian Oceans (e.g., Météo-France) or too cold overall (ECCC).

Examining the ENSO teleconnection, the observed pattern of U200 anomalies (Fig. 3b) is well reproduced in the models for both target seasons (Figs. 3e,h), although it is a little weak for months 1–6. This is consistent with Williams et al. (2023) who reported too-weak ENSO teleconnection in five seasonal hindcasts, including the four we use. Individual model biases in SST and U200 associated with ENSO can also be seen in Fig. S4. Increased precipitation in the tropical Pacific is associated with a typical Gill-type response to enhanced convection in the tropics, with a Rossby wave propagating over the North Pacific and arching over western North America [Pacific North America (PNA) pattern] (Fig. 3c). The models generally overestimate ENSO precipitation anomalies in the western tropical Pacific (Figs. 3f,i), a well-known bias of the coupled general circulation models (Bellenger et al. 2014; Beverley et al. 2023). The bias in Z200x shows a ridge

surrounded by negative anomalies (Figs. 3f,i), suggesting the trough anomaly is larger and less focused than in observations. A northwest–southeast tilt is apparent when looking at the Z200x ENSO teleconnection in the individual models and multimodel ensemble (Fig. S5j) that is not as apparent in observations (Fig. S5a). This tilt was also noted by Williams et al. (2023). It is a seemingly small bias of the ENSO teleconnection but is located right in the region that influences the SWUS. This results in a bias in the U.S. West Coast precipitation associated with ENSO in the models. As shown in Fig. 4, the models are too dry in the Pacific Northwest compared to observations and generally wetter in the SWUS (Fig. 4k). This north–south dipole in ENSO precipitation anomaly in the models results from a slight southward shift in the ENSO-driven atmospheric circulation compared to observations. GPCP is used for observations to include precipitation over the ocean as in the models, but a similar bias is found when using CPC (over land only, not shown).

c. Atmospheric circulation patterns associated with SWUS rainfall

We now investigate the large-scale atmospheric circulation associated with SWUS precipitation, in observations versus seasonal forecasts. Figure 5 shows the regression of P and Z200x on the ONDJFM SWUS precipitation index (defined
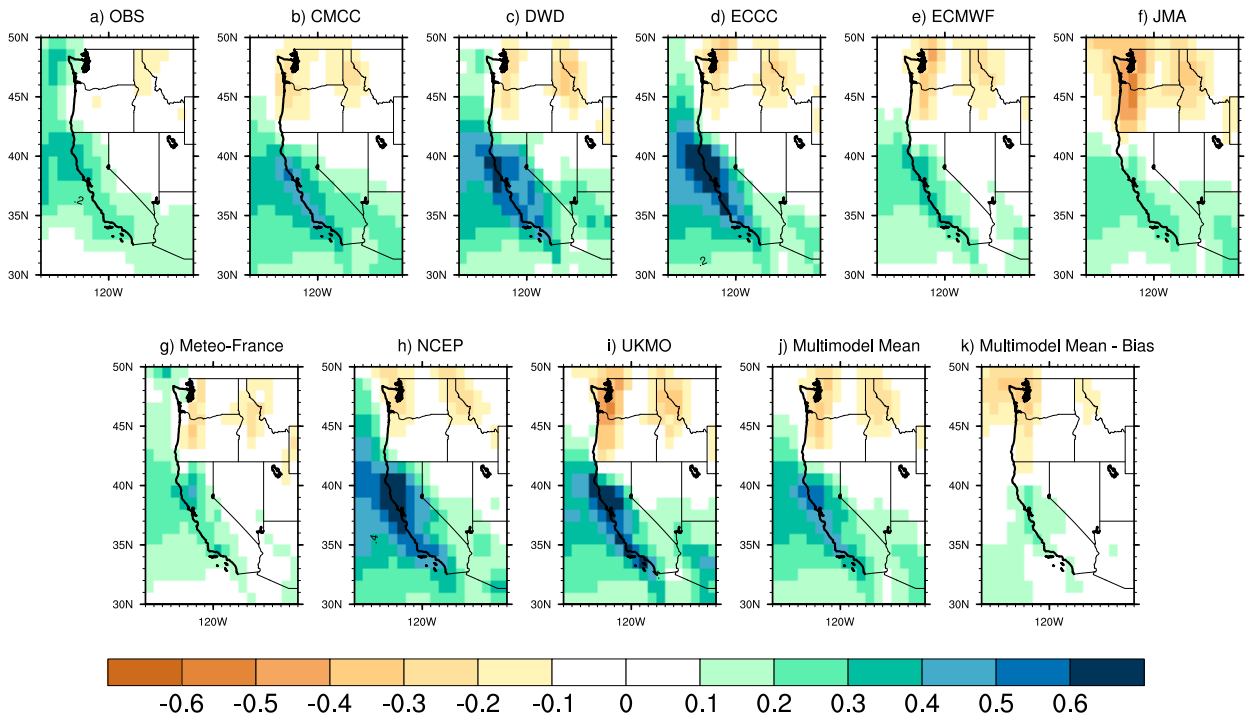
FIG. 4. Regression of U.S. West Coast precipitation (0.1 mm day^{-1} interval) on the Niño-3 index (1993–2016). (a) Observations (GPCP); (b)–(i) month 1–6 hindcasts from the individual models; (j) multimodel ensemble mean; and (k) multimodel ensemble bias.

in section 2b), in observations and in the individual model hindcasts for months 1–6, over the 1993–2016 overlap period (24 years). For the models, the sample size is much larger since we concatenate ensemble members of the hindcasts together. For example, this gives 24 × 40 = 960 years for CMCC, since 40 ensemble members are provided for this model (Table 1). In observations, seasonal SWUS precipitation is associated with a trough anomaly in the eastern North Pacific (Fig. 5a, contours), which directs storms and rainfall over the region. It also coincides with high precipitation in the east/central tropical Pacific (Fig. 5a, shading) and moderate El Niño SST anomalies in the tropical eastern Pacific (not shown), reflecting the moderate relationship between ENSO and high SWUS precipitation.

However, the Z200x anomalies of Fig. 5a are more complex than the ones associated with ENSO (Fig. 3c), suggesting a diversity of influence on SWUS P. In particular, we identify an arching wave train originating in the EAJS, with a ridge centered off the coast of Japan, that resembles midlatitude zonal wave trains discussed in D24. Compared to observations, the models simulate deeper Z200x anomalies in the ENP region (Fig. 5k). They also exhibit simpler structures in the Z200x patterns, typical of the PNA-like pattern with less of the zonal/arching wave train. This general view is confirmed by the multimodel ensemble mean (Fig. 5j) and in the multimodel bias that exhibits a zonal wave train in the North Pacific and in the high latitudes (Fig. 5k). Note that a similar multimodel bias is already present in the month 1 prediction (not shown).

A limitation of regression analysis is that it does not address nonlinearity in the statistical linkages. That is, in the present case, the regression analysis includes drivers of wet, neutral, and dry conditions in the SWUS. To address nonlinearity, we performed a composite analysis shown in Fig. 6 that groups years exhibiting more than one standard deviation in the SWUS P index. Compared to Fig. 5, we analyze the extended 1948–2023 period to maximize sample size (using CPC for the SWUS precipitation index) and composite SST rather than precipitation along with Z200x (because unlike global precipitation, SST is available over the 1948–2023 period). This extracts 15 years from the 76 ONDJFM seasons over 1948–2023 in observations and 37–155 in the hindcasts (from 240 to 960 seasons). The Z200 composite patterns resemble the regression patterns of Fig. 5, which verifies that the results are robust using different methods and periods and relatively linear (i.e., regression analyses reflect what happens during wet SWUS years). Interestingly, the contrast between observations and the models is more pronounced here, as seen in Fig. 6a where a clearer zonal wave emerges in observations in the high latitudes. In the models, once again the signal is reminiscent of the quadrupole from the PNA pattern, with no zonal wave train in higher latitudes (Fig. 6j). An exception is Météo-France that exhibits a ridge over the Aleutians Islands as in observations (Fig. 6g).

Because ENSO is a prominent signal associated with SWUS P in these analyses, we then remove its influence in regression patterns similar to Fig. 5. For this, we regress both the SWUS P index and the fields onto the Niño-3 index and
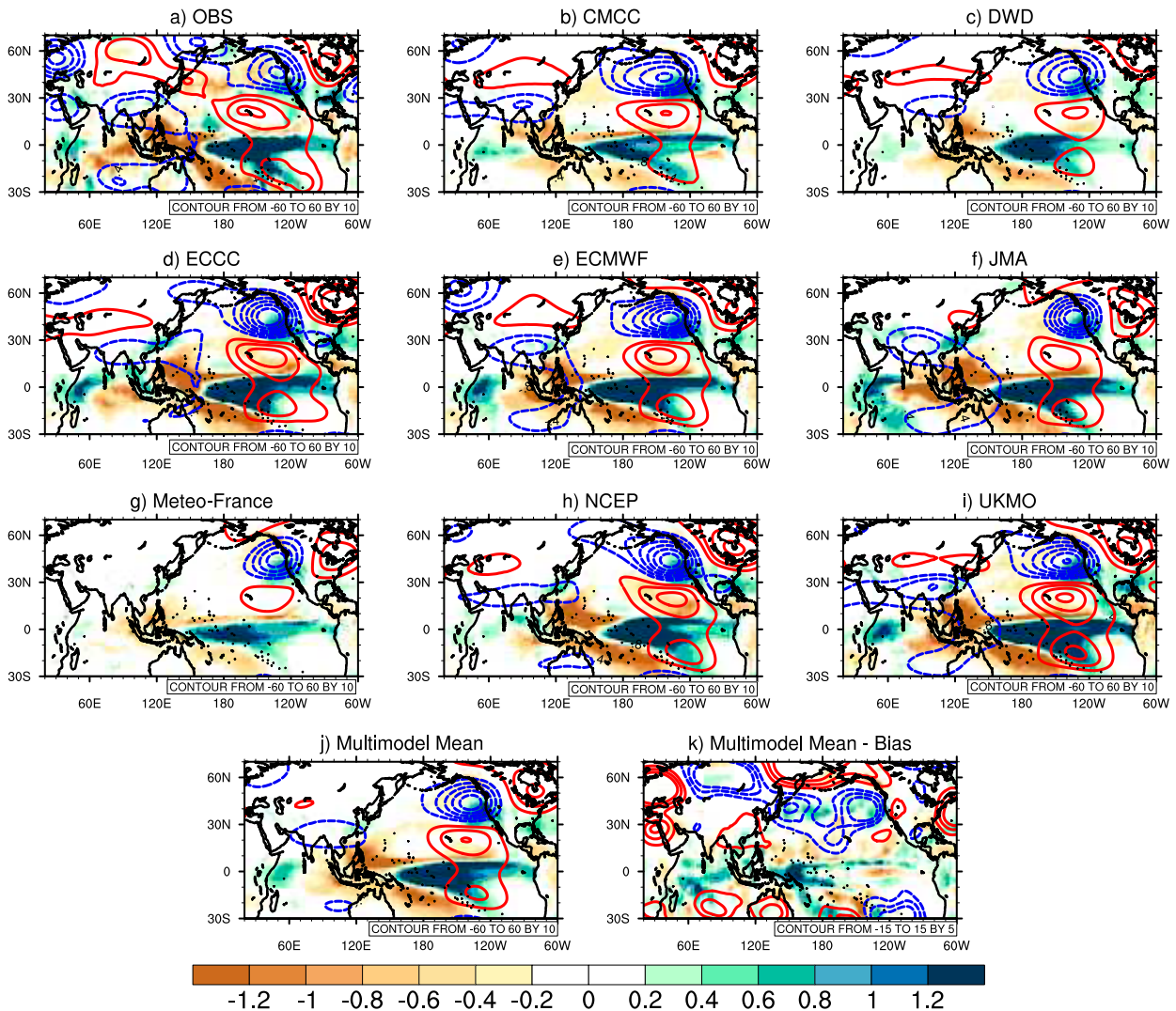
FIG. 5. Teleconnection associated with SWUS *P*. (a) Regression of ONDJFM precipitation (GPCP, shading, 0.2 mm day^{-1} interval) and Z200x (ERA5, contours, 10-m contour interval) on the SWUS precipitation index, for the 1993–2016 period. (b)–(i) As in (a), but for months 1–6 of the individual forecast systems (1993–2016 period too). (j) As in (a), but for the multimodel ensemble mean. (k) Bias of the multimodel ensemble, i.e., difference from observations [(j) minus (a), 5-m contour interval for Z200x]. Red contours are for positive Z200x anomalies, and blue contours are for negative Z200x anomalies.

examine the residuals (Fig. 7). By design, the positive precipitation anomaly associated with ENSO in the tropical Pacific disappears. In observations (Fig. 7a), the residuals of the Z200x anomalies show a wave train over the North Pacific and North America, with a pronounced trough centered over the ENP region, resembling zonal patterns that drive wet SWUS conditions independently of ENSO (Wang et al. 2017). In the models, generally the residual wave pattern still resembles an ENSO-like teleconnection, with a meridional (PNA-like) wave characterized by a ridging anomaly in the subtropical Pacific and a trough in the North Pacific (Fig. 7j). Compared to observations, this results in low-pressure/trough anomalies that are less localized in the ENP region and extended to the west over the North Pacific (Fig. 7k), with less

ridging in the central North Pacific as in observations. An exception is JMA that shows a ridge–trough–ridge pattern in the North Pacific (Fig. 7f). Here too, similar biases are already present in the month 1 prediction (not shown), suggesting that model biases affect the hindcasts early on in the runs.

Overall, these results seem to support the idea that the forecast models, and coupled climate models in general, tend to overestimate the influence of meridional wave trains on SWUS seasonal precipitation (directly associated with ENSO or not) to the detriment of zonal wave trains (Dong et al. 2023; D24). This is of course under the assumption that the signals we extract in observations are robust, for which we have one realization only, i.e., less robust than for the models. However, results from the following sections support this finding.
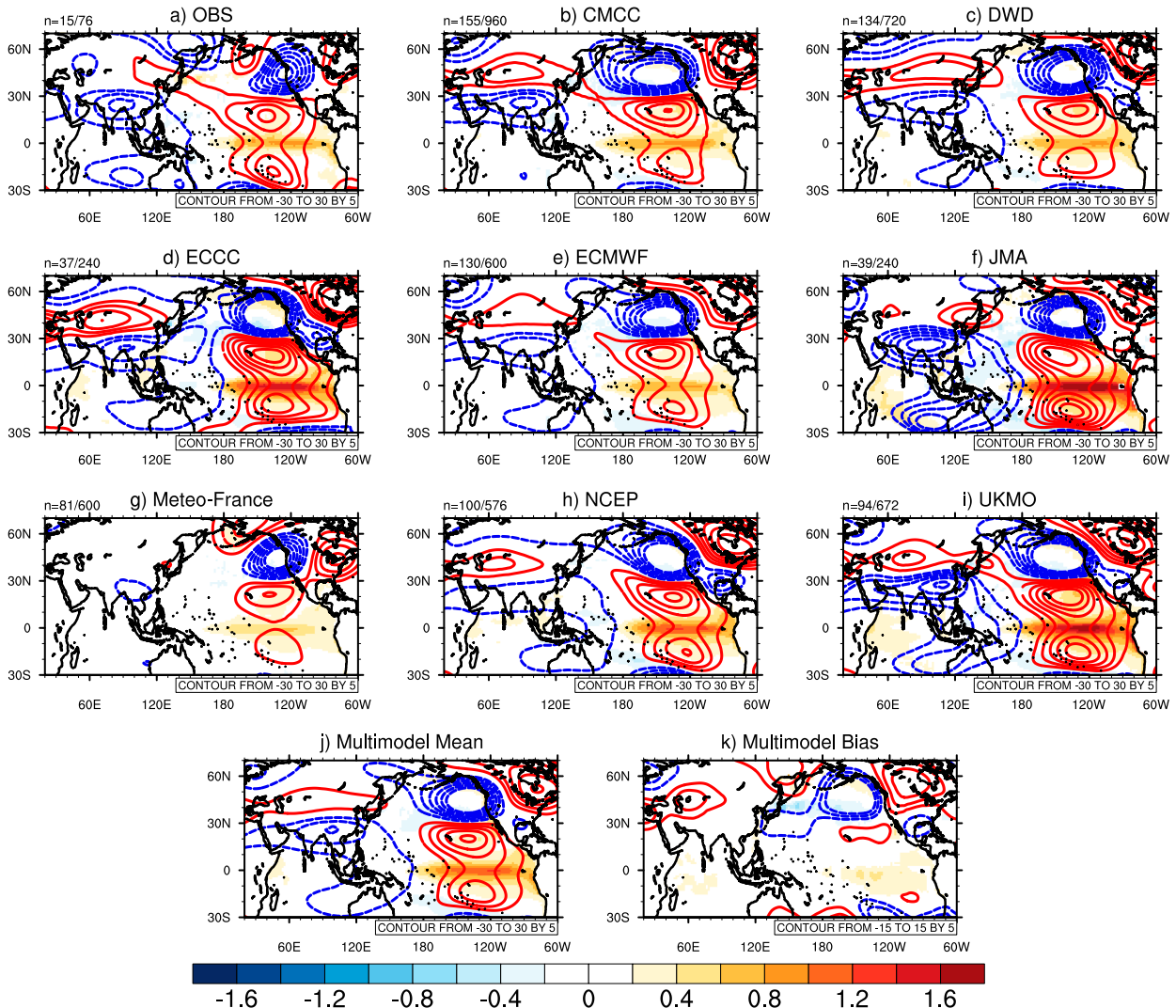
FIG. 6. Teleconnection associated with high SWUS P. (a) Composite of ONDJFM SST (shading, 0.2°C interval) and Z200x (ERA5, contours, 5-m contour interval) for the 15 years with a high (>one standard deviation) SWUS precipitation index, over the 1948–2023 period. (b)–(i) The same composite as in (a), but for model years with a high (>one standard deviation) SWUS precipitation index, out of all the ensembles of month 1–6 predictions from each forecast system (full hindcast period). (j) As in (a), but for the multimodel ensemble mean. (k) Bias of the multimodel ensemble, i.e., difference from observations [(j) minus (a)]. Red contours are for positive Z200x anomalies, and blue contours are for negative Z200x anomalies. The number of years/hindcasts selected for the composite, versus the total number of years in the dataset, is given in the upper left of each panel.

d. Underestimation of zonal wave trains in the models

The previous section suggests that the seasonal models do not capture the influence of zonal wave trains on seasonal SWUS precipitation as in observation. Here, we explore whether this may be a general bias in the models by measuring how they represent these seasonal zonal wave trains, versus observations, without any focus on ENSO or SWUS signals. For this, we use the North Pacific waviness index described in section 2b, which we calculate for ERA5, the seasonal models, and also the numerical experiments described in section 2c. This index measures the waviness (or meanders) of the atmospheric flow at 200 hPa using the zonal gradient of

V200. For each dataset, one value per season is retrieved, and the distribution of these values is plotted in Fig. 8 using a box-and-whisker plot representation. The distribution of the index is relatively similar in all the datasets, with the exception of extreme values being more frequent in the model data, which is expected from the much larger sample size. ONDJFM 2017, which we discuss in the next section, is the highest value on record in ERA5, making it a textbook example of a prominent and seasonal zonal wave train over the North Pacific. For comparison, the 1983 value is provided, showing that a strong El Niño year does not typically lead to a high value of this index. When compared to model distribution, from both
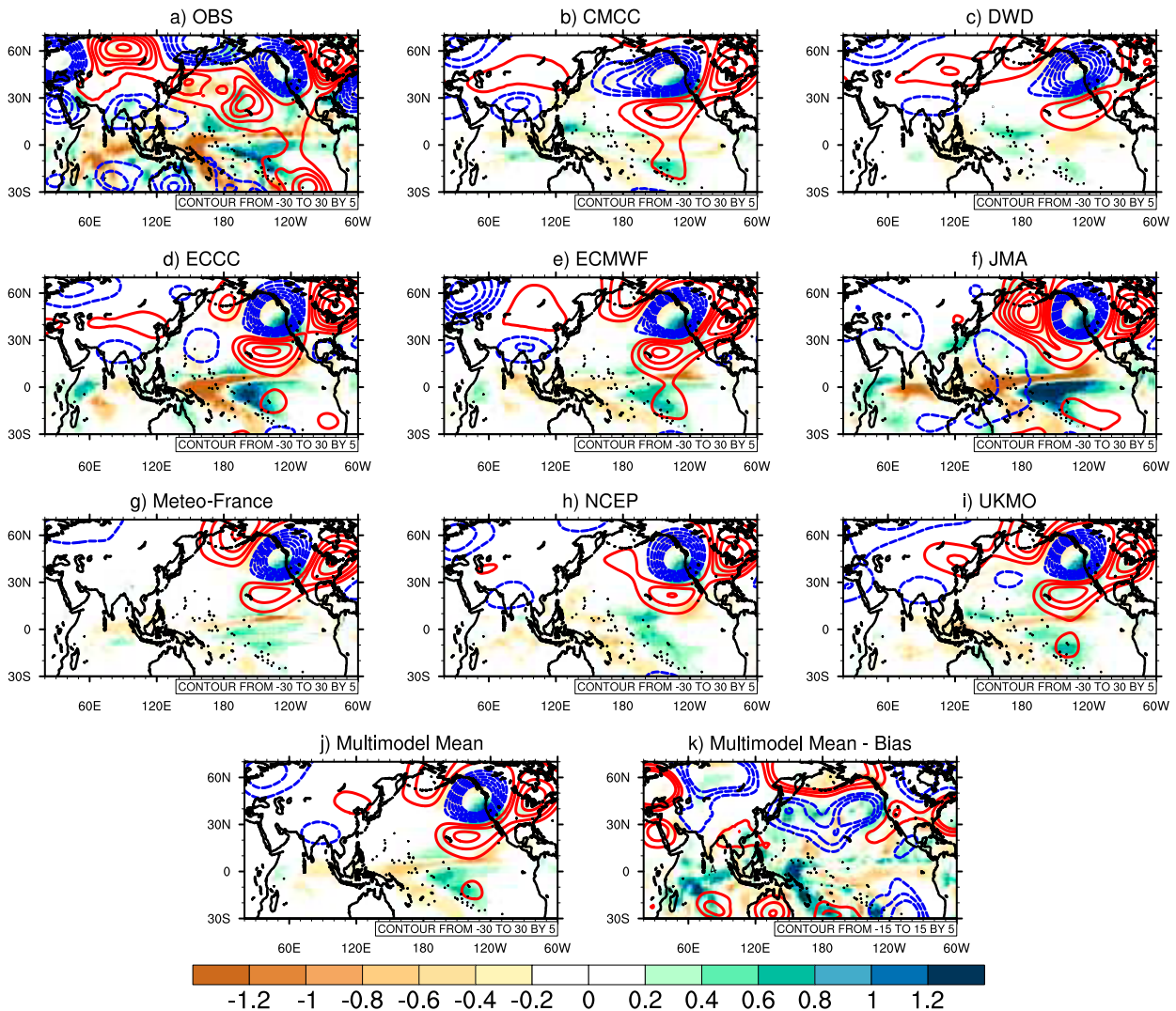
FIG. 7. As in Fig. 5, but after removing the influence of ENSO, through a regression of the SWUS *P* index and the fields onto the Niño-3 index to retain residuals only. The contour interval is 5 m for Z200x. Period: 1993–2016.

the seasonal hindcasts and our perturbation experiment, 2017 represents an extreme case, close to the upper limit of the model distribution.

A question that comes to mind is whether the atmospheric patterns associated with high values of the North Pacific waviness index are similar across datasets. This is answered in Fig. 9 that shows composites of V200 and Z200x onto high values of the index (greater than 1.5 standard deviations) for ERA5 and the seasonal hindcasts. The procedure selects 11 years in ERA5 (out of 84 years, 1940–2023) and from 18 to 75 in the hindcasts that have considerably larger sample sizes. In support of section 3c, there is a substantial difference between the models and observations. High waviness of the North Pacific flow in the models is mostly associated with a quadrupole that resembles the PNA, or arching wave, pattern with a trough in the subtropical North Pacific followed by a ridge–trough–ridge pattern further north. This trough is much weaker

in ERA5, and the ridge–trough–ridge pattern in higher latitudes is embedded in a large-scale zonal wave train that originates over India, at the entrance of the EAJS, with also a second wave train in the high latitudes. Similar analyses over the 1993–2016 period for observations yield comparable results (not shown). This points to a fundamental bias in the models' representation of atmospheric variability in the North Pacific: At seasonal time scales, they generally underestimate the probability that high-wavenumber zonal wave trains may linger in the North Pacific, as happened during WY 2017.

To investigate why, we perform a similar analysis to D24 and examine how the model mean state biases affect zonal Rossby wave propagation. This is done by calculating the stationary wavenumber field for reanalysis and the hindcasts and evaluating linear Rossby wave propagation using ray tracing (see D24 for details on the method). First, we compare the stationary wavenumber field at 200 hPa between observations
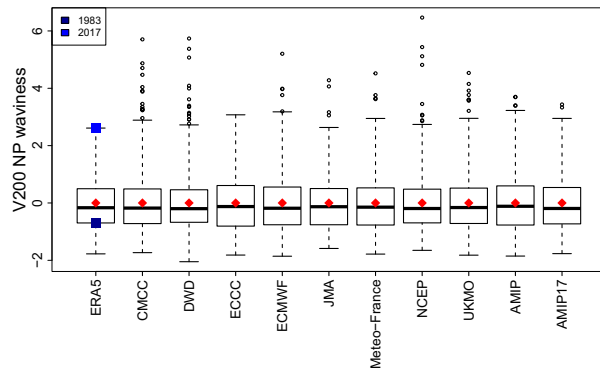
FIG. 8. Distribution of the seasonal ONDJFM North Pacific waviness index (from V200), in ERA5 (1940–2023, 84 seasons), CMCC (1993–2016, 960 seasons), DWD (1993–2019, 810 seasons), ECCC (1993–2020, 280 seasons), ECMWF (1981–2016, 900 seasons), JMA (1993–2016, 240 seasons), Météo-France (1993–2018, 650 seasons), NCEP (1993–2016, 576 seasons), UKMO (1993–2016, 672 seasons), AMIP (1978–2016, 390 seasons), and AMIP17 (300 seasons). The boxplots indicate the median and upper and lower quartiles of the distribution. The whiskers indicate the minimum and maximum values, with outliers in circles (outliers are values beyond two interquartile ranges from the upper-quartile range). The ensemble mean (zero by construction) is marked by a red diamond. For ERA5, the values of the index for 2017 and 1983 are marked by blue squares.

and hindcasts (Fig. 10), focusing on the DJF season (months 3–5 of the September/1 October initialized hindcasts) since this is the season when the basic-state jet and tropics–extratropics teleconnection are the strongest. Two waveguides of high stationary wavenumber exist in the North Pacific, one associated with the EAJS, with regions of forbidden propagation on the northward and southward flanks, and another one in the eastern North Pacific (Fig. 10a).

The two distinct waveguides connect in the central subtropical Pacific, and the EAJS waveguide extends to the northeast, allowing for wave propagation toward North America. There is a tendency for the models to merge these two waveguides, reducing the channel of high-wavenumber propagation toward the western coast of North America. This is similar to the bias that was identified in version 2 of the Community Earth System Model large ensemble (CESM-LENS; Kay et al. 2015) by Dong et al. (2023), and we propose that it reflects an overestimation of the El Niño/SWUS P relationship in the models that is directly related to biases in the basic flow. As can be seen in Fig. 10, biases in U200 (overlaid in black contours) and in particular a too-strong and elongated jet circulation in the subtropical North Pacific lead to a retraction of the midlatitude waveguide and a strengthening of the absolute vorticity gradient in the subtropics (Dong et al. 2023).

While we qualitatively anticipate that this leads to a southward deflection of Rossby waves, we can quantitatively test this using ray tracing, initiating rays with initial zonal wavenumber $k = 5$, the dominant wave scale in the waveguide during DJF (Branstator and Teng 2017), at 1° intervals from 75° to 140°E along a latitude band at 30°N. At each location, two

rays are initiated, with either a positive meridional wavenumber or a negative meridional wavenumber, totaling 132 rays. We then integrate their path as described in D24 and count the frequency of ray propagation into the ENP region at the exit of the EAJS (defined as crossing eastward over 230°E between the latitudes 30° and 60°N), where they have the potential to influence SWUS precipitation. This is done using the observed U200 basic state (Fig. 11a), each individual model's U200 basic state (Figs. 11c–j), as well as the multimodel U200 basic state computed from the multimodel ensemble (Fig. 11b). We find that 42% of these Rossby waves propagate into the ENP domain under the ERA5 basic state, compared to 33% in the multimodel ensemble. This indicates that the seasonal models on average may underestimate the influence of zonal wave trains on SWUS precipitation, especially as basic-state biases grow with lead time, since too many of these waves may be deflected southward in the east Pacific. This is especially true for two models that exhibit significantly lower frequency of propagation in the ENP domain, Météo-France, and NCEP, which are also the models with the most pronounced U200 dipole bias in the North Pacific (Figs. 10h,i). This is also consistent with conclusions from D24, as a similar bias is found at weeks 5–6 in the S2S hindcasts, when models are no longer (or minimally) influenced by initial conditions.

e. Case study: The 2016–17 winter

A particularly interesting year for seasonal prediction is the WY 2017. Following a disappointing El Niño 2016 WY that did not bring the expected rain (Kumar and Chen 2017), California experienced its second wettest year on record, narrowly following the "monster El Niño" 1983 WY.[3] Both the 2016 and 2017 WYs were not predicted by the ensemble mean seasonal forecast ensembles (Kumar and Chen 2017; Singh et al. 2018), although the 2016 WY has been shown to be within the envelope of possible forecast outcomes (Chen and Kumar 2018). The anomaly of precipitation in ONDJFM 2017 can be seen in Fig. 12a, using the CPC data. Most of the western United States was wetter than normal, in particular CA, with this WY ending the severe 2011/16 drought in the state. We only have three models that include WY 2017 in the C3S seasonal hindcasts, DWD, ECCC, and Météo-France. Their performance in predicting P and SLP is shown in Figs. 12b–d, with the multimodel ensemble prediction in Fig. 12e. Although the three models tend to predict wetter-than-normal conditions in the northwest United States, they never meet the amplitude of observations and they miss their extent, especially the extension of the excess in precipitation to the SWUS. Our set of hindcasts does not include 2017 for UKMO, but according to Singh et al. (2018), it also failed to predict the observed precipitation for that season. Despite forecast failure by the ensemble, the 2017 SWUS precipitation anomaly falls within the range of predicted values by individual hindcasts from the multimodel ensemble (Fig. S6). It

---

[3] https://cawaterlibrary.net/document/water-year-2017-what-a-difference-a-year-makes-2/.
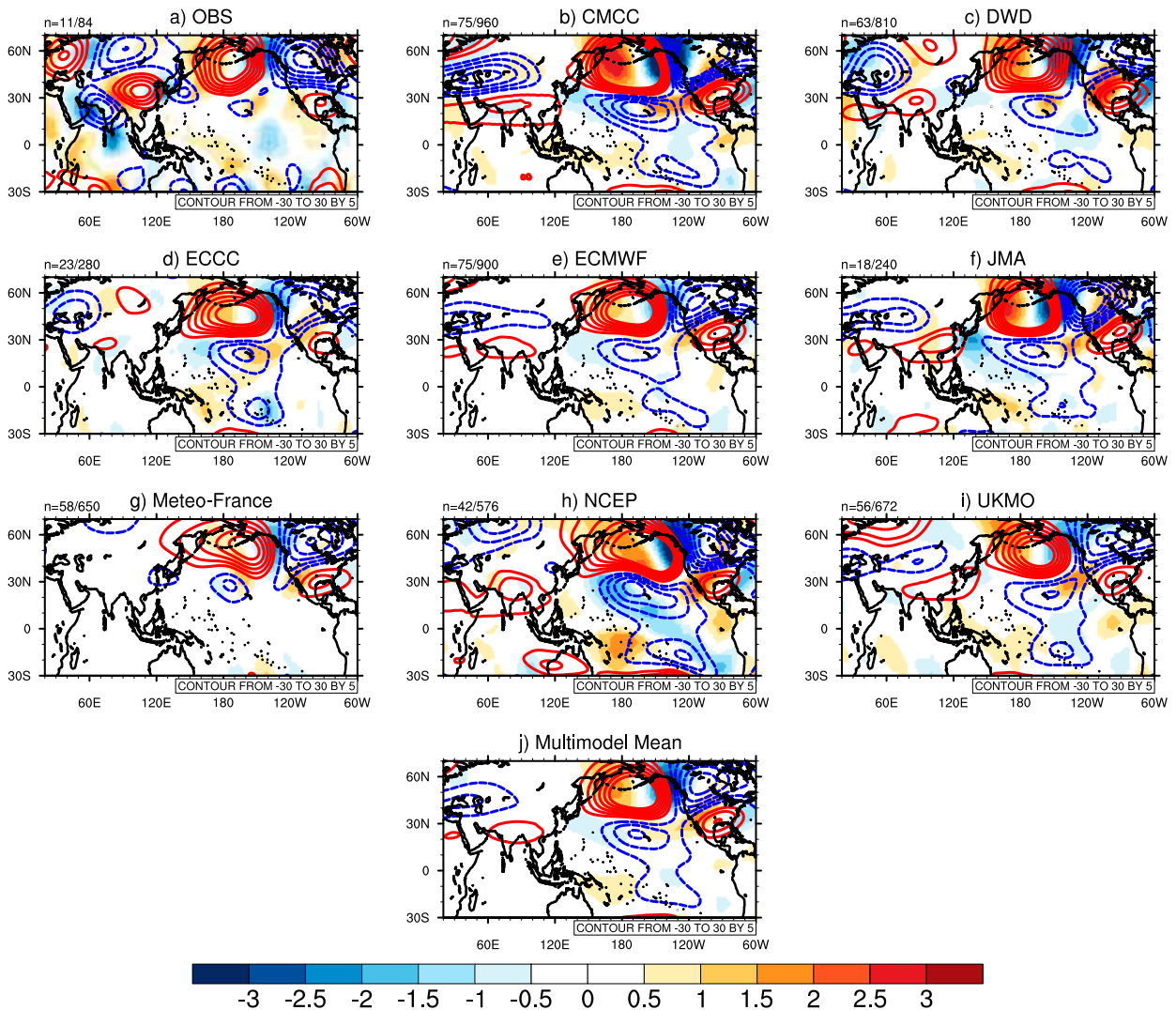
FIG. 9. Composite of V200 (shading, 0.5 m s^{-1} interval) and Z200x (contours, 5-m contour interval) for seasons with a value of the NP waviness index greater than 1.5 standard deviation for (a) ERA5, (b) CMCC, (c) DWD, (d) ECCC, (e) ECMWF, (f) JMA, (g) Météo-France, (h) NCEP, (i) UKMO, and (j) mutlimodel ensemble mean. Red contours are for positive Z200x anomalies, and blue contours are for negative Z200x anomalies. The number of years selected for the composite, versus the total number of years in the dataset, is given in the upper left of each panel.

represents the 94th percentile of predicted values by the 65 available hindcasts for that season (30 from DWD, 10 from ECCC, and 25 from Météo-France). This points out that the observed anomaly is within the range of model variability; i.e., internal variability alone can cause the forecast miss, rather than model deficiencies (in line with Chen and Kumar 2018).

The wet WY was driven by the predominance of a favorable atmospheric pattern throughout the ONDJFM season, i.e., a low-pressure trough in the ENP that directed atmospheric rivers toward California, causing abundant precipitation over the state. The low-pressure trough in the ENP was a local marker of a larger-scale stationary wave, with alternating troughs and ridges over the North Pacific (Wang et al. 2017). This can be seen in Fig. 13, which displays the SST

(HadISST) and Z200x (ERA5) anomalies for ONDJFM 2017. The atmospheric circulation exhibits a remarkably consistent circumglobal zonal wave train. The wave train appears to originate in the EAJS and propagate downstream over the North Pacific, with a pronounced trough–ridge dipole centered over the U.S. West Coast. As can be seen in the SST anomalies, no pronounced ENSO signal was observed in the tropical Pacific. The ONDJFM hindcasts initialized in September/1 October (months 1–6) are successful in predicting the SST (Figs. 13b–e, shading), but they miss the zonal wave train observed in the North Pacific (Figs. 13b–e, contours). The 2017 WY is a good example of the current limits of seasonal forecasting. It would have been most beneficial to predict this season as it was extreme, but this seems to be beyond the capability of the current forecast systems.
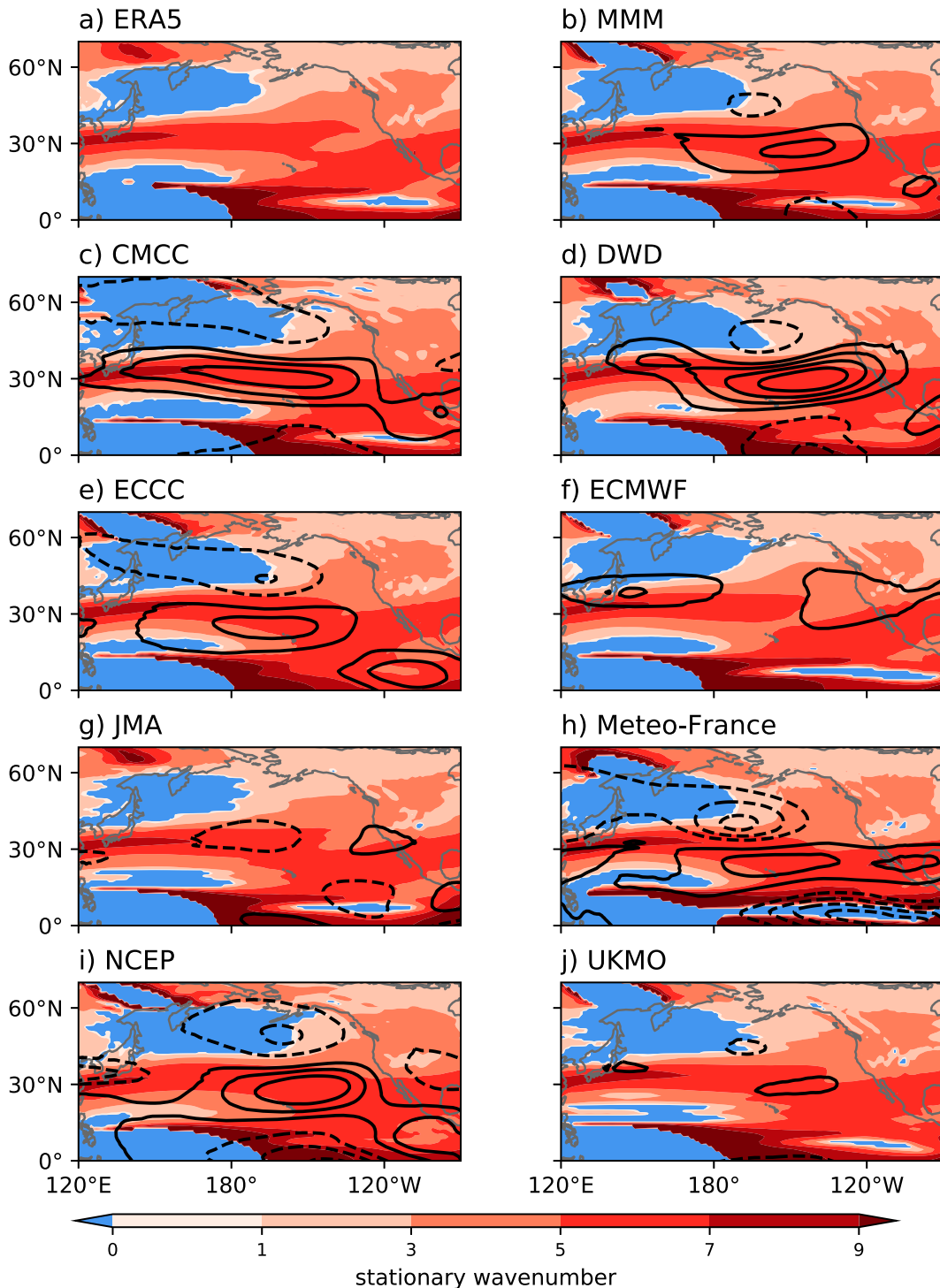
FIG. 10. DJF stationary wavenumber in (a) ERA5 and in DJF (months 3–5 in the hindcasts) from the (b)–(j) models, along with U200 biases (contour). Contour interval is 3.0 m s^{-1}. Zero contour level is omitted. Imaginary values of stationary wavenumber are shaded in light blue.

To explore physical mechanisms and potential predictors that may have driven the pronounced seasonal zonal wave train and CA precipitation, we turn to the AMIP-type perturbation experiments described in section 2c. The 100-member ensemble of runs branched on 1 October 2016 is averaged to extract the ensemble mean and response to the prescribed forcing. The ONDJFM 2017 response is then compared to observations. In Fig. 14a, we show the velocity potential (VP250,
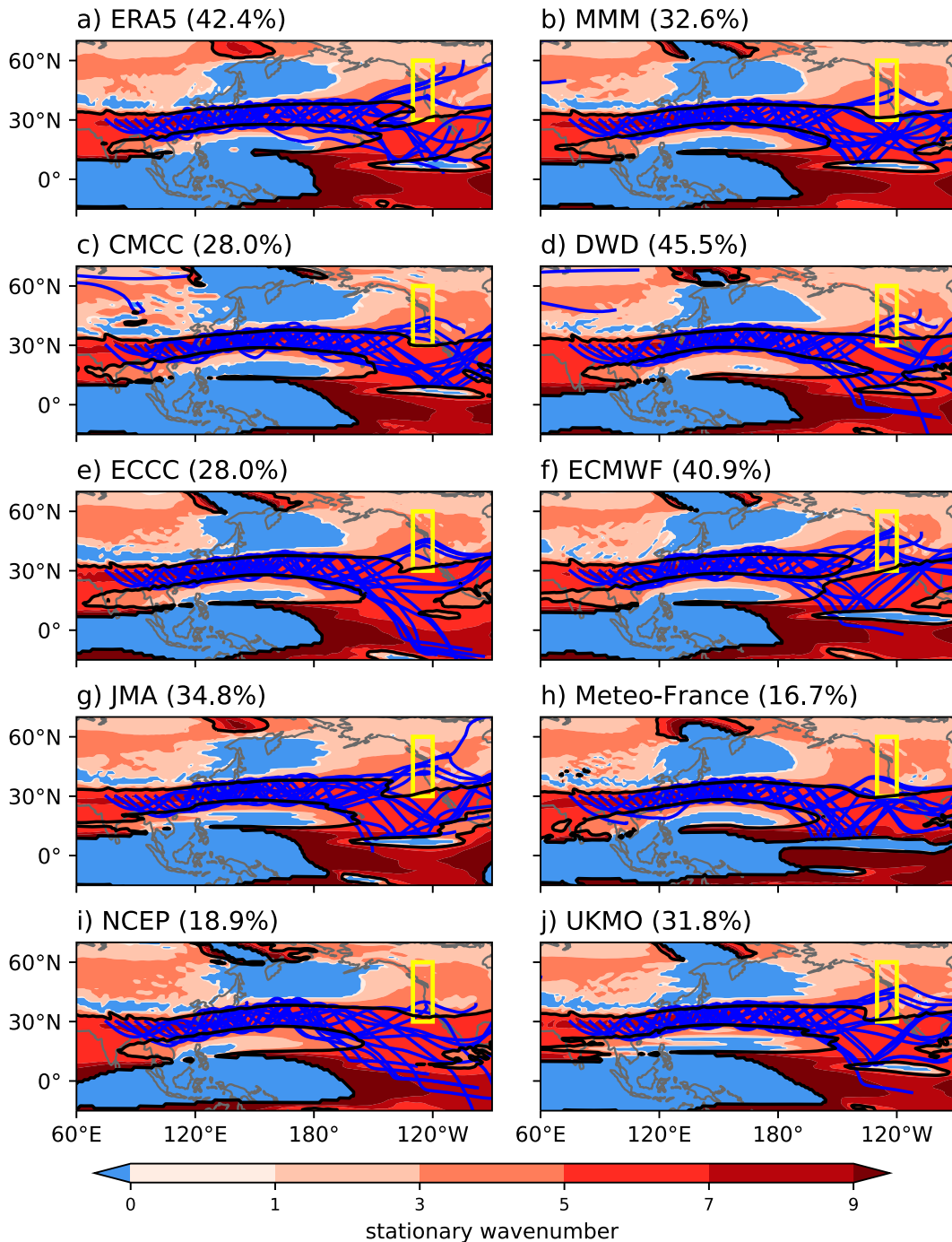
FIG. 11. DJF stationary wavenumber for (a) ERA5 and month 3–5 forecast climatologies from the (b)–(j) models. The black contour is stationary wavenumber-5 level. Blue lines represent a subset of rays initialized in the EAJS with $k = 5$. The yellow box indicates the region used for ENP propagation frequency, which is shown in each subplot title.

shading/black contours) and meridional wind (V250, red/blue contours) anomalies at 250 hPa from MERRA-2 (because the runs are nudged toward MERRA-2). The North Pacific wave train visible in the V250 is consistent with Fig. 13a, as expected. The 250-hPa velocity potential is a marker of large-scale vertical motion in the atmosphere, often used to characterize tropical convection. Figure 14b shows the response in the AMIP17 experiment, i.e., the influence of observed SST/SIC anomalies. For VP250, only anomalies that are statistically significant at the 95% confidence level are shaded.
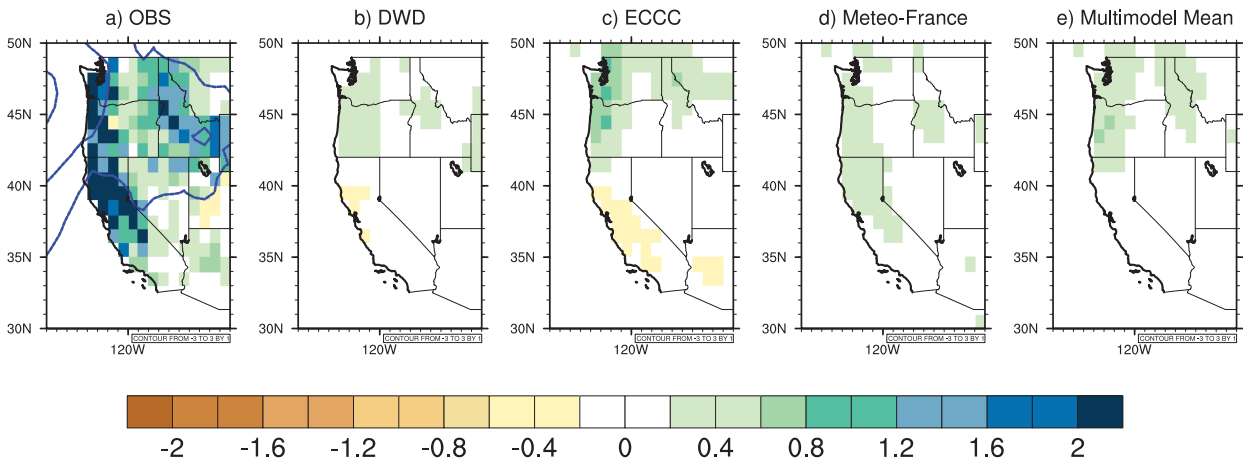
FIG. 12. The 2017 seasonal (ONDJFM) P anomaly (shading, 0.2 mm day^{-1} interval) and SLP anomaly (contours, 1-hPa contour interval), relative to 1993–2016. (a) Observations (CPC/ERA5), (b) ensemble mean prediction from DWD, (c) ensemble mean prediction from ECCC, (d) ensemble mean prediction from Météo-France, and (e) multimodel ensemble mean prediction.

Statistical significance for the ensemble mean of each nudging experiment is estimated using 1980–2017 ONDJFM seasonal anomalies from the AMIP experiment as the control group. As can be seen in the VP250 anomalies (shading), prescribing SST allows for a fairly accurate representation of large-scale convection anomalies in the tropics (Walker circulation), as measured by the anomaly pattern correlation of 0.61 (area weighted, comparing VP250 anomalies to observations in the shown domain). Although a wave train originating in the EAJS is forced in the North Pacific (V250 contours), it is much weaker than in observations. The corresponding precipitation anomaly (Fig. 14f, compared to GPCP precipitation to include the ocean in Fig. 14e) resembles the prediction of the seasonal forecast models in Fig. 13, with slightly wetter-than-normal conditions in the northwest and dry conditions in the SWUS. This is consistent with the fact that the forecast models mostly rely on SST for seasonal prediction.

After prescribing tropical variability through the nudging of the tropical troposphere (Fig. 14c; AMIP-TROP17), the accuracy of the VP250 anomalies is refined, and the zonal wave train is reinforced. However, it does not exhibit the exact same propagation and structure as in observations, resulting in a different location for the ENP trough, and the precipitation anomaly is actually worse than for AMIP17, with overall dry conditions in contrast to observations (Fig. 14g). Finally, by adding nudging of Arctic tropospheric variability in AMIP-TRHL17, we retrieve patterns that are closer to what was observed in 2017. The zonal wave train is much closer to observations (Fig. 14d), as is the precipitation anomaly (Fig. 14h), although it is still too dry in the SWUS. In the North Pacific, the difference between AMIP-TRHL17 and AMIP-TROP17 is highly significant, at the 99% confidence level using the Student's t test (not shown). A similar result is obtained when nudging Arctic variability alone (Fig. S7), such that for this case study, tropical nudging is not necessary in order to represent the North Pacific zonal wave train and the western U.S. precipitation anomaly. This means that the climate anomaly can be explained by a combination of SST tropical forcing plus high-latitude atmospheric variability. This is remarkably consistent with Singh et al. (2018), who found that high-latitude variability was an important driver of CA precipitation in WY 2017. In particular, they found that forecast ensemble members that successfully predicted CA precipitation were the ones that correctly predicted the phase of the Arctic Oscillation (AO). By nudging the Arctic domain, we prescribe AO variability in our AMIP-TRHL17 experiment, and in agreement with their study, this leads to a better representation of precipitation anomalies. These results point to a role for tropical SST in generating a Rossby wave through convection anomalies in the vicinity of the EAJS. The wave train then propagated along the EAJS and its exit region over the North Pacific, being refined by high-latitude variability along its path, leading to the prominent seasonal trough–ridge anomaly over the U.S. West Coast. A limitation of this analysis is that the nudging domain starts at 60°N, which includes a portion of the observed trough–ridge dipole in the North Pacific. This makes interpretation difficult, as the improved representation of the wave train may simply be the result of nudging the northern part of these centers of action. Still, this does not preclude that high-latitude variability was important in the propagation of this wave train.

4. Conclusions

Following up on D24 that focused on S2S teleconnections and forecast models, in this study we explore potential model biases that may hamper the skill of seasonal forecasts when trying to predict seasonal SWUS precipitation. Eight sets of hindcasts from the C3S ensemble are analyzed, focusing on the ONDJFM season, month 1 prediction (average of monthly forecasts for October–March months), and month 1–6 prediction (forecast of the ONDJFM average after September/1 October initialization). In line with previous studies that reported low forecast skill for predicting SWUS precipitation, we find that the multimodel forecast ensemble explains a maximum of a quarter of the SWUS precipitation variance over 1993–2016 ($R = 0.52$), comparable to correlations with a linear ENSO
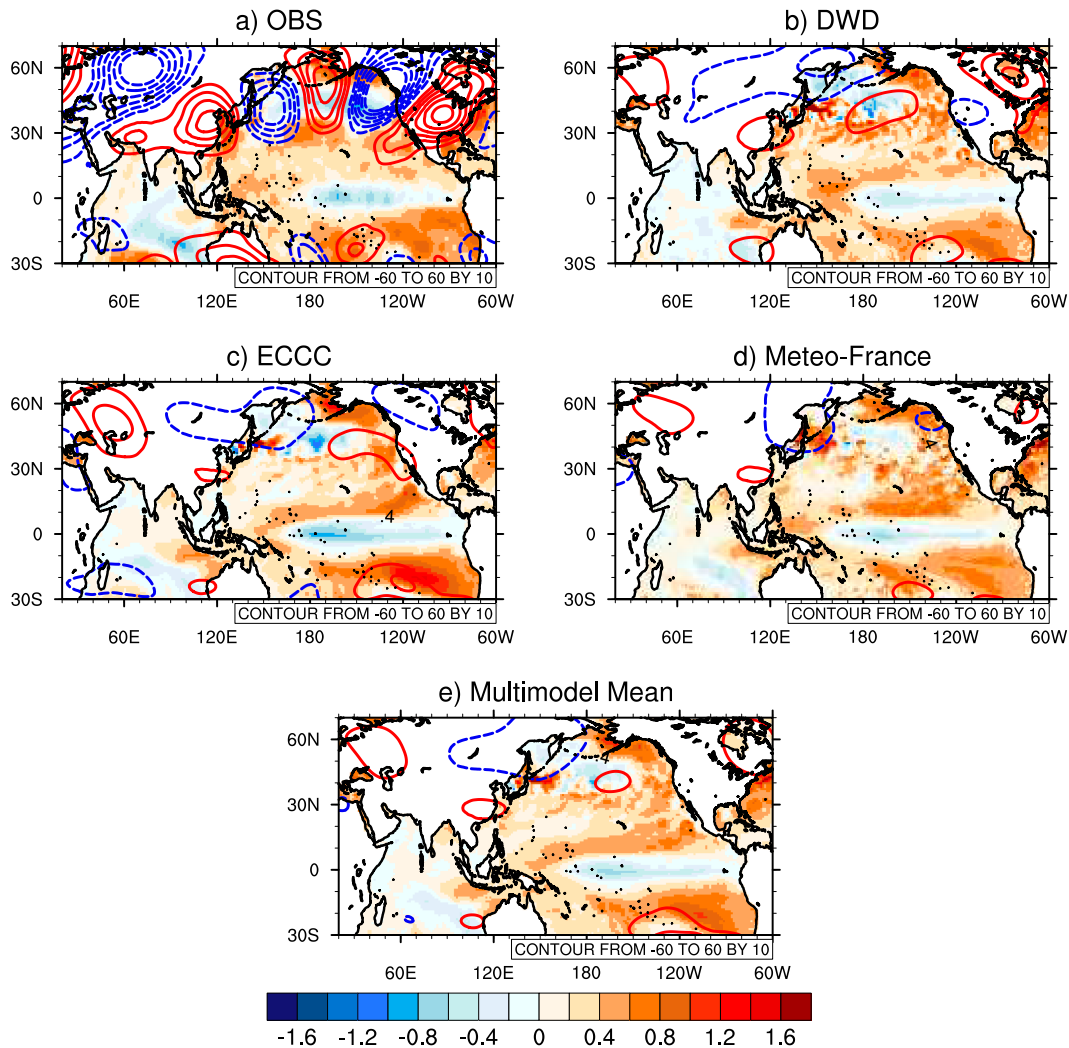
FIG. 13. The 2017 seasonal (ONDJFM) SST anomaly (shading, 0.2°C interval) and Z200x anomaly (contours, 10-m contour interval), relative to 1993–2016. (a) Observations (HadISST/ERA5); (b) ensemble mean prediction from DWD, for months 1–6; (c) as in (b), but for ECCC; (d) as in (b), but for Météo-France; and (e) as in (b), but for the multimodel ensemble mean prediction (3-model average).

predictor (e.g., Jiang et al. 2022). While low forecast skill is probably inherent due to atmospheric internal variability and low signal-to-noise ratio (Kumar and Chen 2020), the forecast models do contain significant errors that may detract from predictive skill. The most noticeable and recurrent is a bias in the subtropical Pacific jet circulation, represented by too-zonal and strong westerly circulation in the eastern subtropical North Pacific. The jet bias is reinforced with lead time, but it is already present in month 1, i.e., within a few weeks of initialization. The models also simulate a too-weak and shifted ENSO teleconnection at seasonal lead times (consistent with Williams et al. 2023), which induces a southward shift of the associated precipitation anomaly along the U.S. West Coast.

An important conclusion from this study is that seasonal forecast models rely too much on ENSO-like meridional wave trains to drive seasonal SWUS precipitation, underestimating the influence of zonal wave patterns. While in observations, SWUS is influenced by both tropics–extratropics/PNA-like and zonal/circumglobal wave trains, the forecast models mostly exhibit ENSO/PNA-like patterns in our analyses. A Rossby ray-tracing analysis illustrates how model bias in the atmospheric basic state affects the propagation of wavenumber-5 wave trains along the EAJS, leading to errors and underestimation of their propagation to the north. This is similar to results from D24 where the same analysis was performed using S2S forecast models (5–6 weeks after initialization). The tendency for the model to overpredict the influence of meridional, ENSO-like, wave trains versus the influence of zonal wave trains on SWUS precipitation was also found in the CESM2 large ensemble (Dong et al. 2023). We suggest this is a common bias affecting not only S2S/seasonal forecast models but also the current generation of ocean–atmosphere coupled models in general.
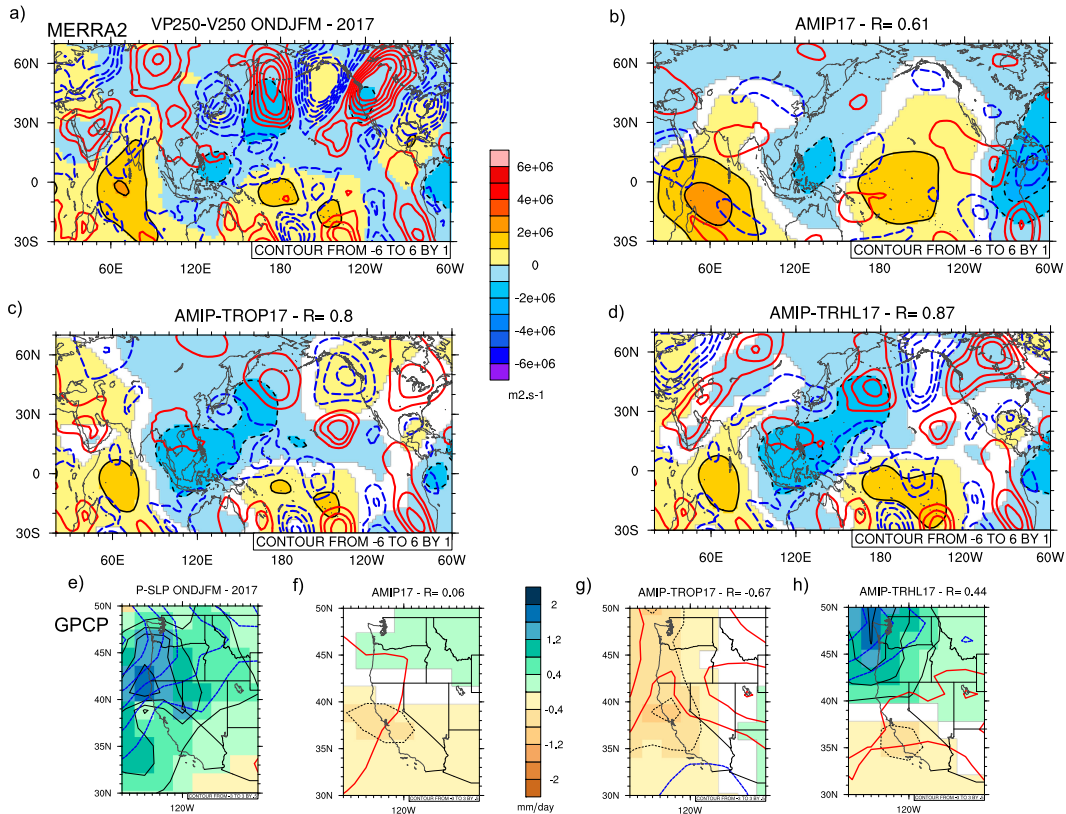
FIG. 14. The 2017 seasonal (ONDJFM) VP250 anomaly (shading and black contours, 1×10^6 m^2 s^{-1} contour interval) and V250 anomaly (contours, 1 m s^{-1} contour interval), relative to 1980–2017. (a) Observations (MERRA-2); (b) response in AMIP17; (c) response in AMIP-TROP17; (d) response in AMIP-TRHL17; and (e)–(h) corresponding P (0.4 mm day^{-1} contour interval) and SLP anomaly (0.5 hPa contour interval); GPCP and ERA5 are used for observations. The anomaly pattern correlation between observations and the experiment is given on top of each panel, for VP250 and P. For the simulations, anomalies that are significant at the 95% confidence level are shaded.

A case study of the unexpectedly wet 2017 WY reveals how challenging such years are for seasonal forecasters. In the absence of a well-defined ENSO anomaly, a pronounced zonal Rossby wave train persisted over the North Pacific during the season directing multiple ARs over CA and resulting in abundant precipitation. This anomaly was not predicted by the forecast ensembles, as illustrated by analyses of the hindcasts that include 2017. Our hierarchy of WACCM4 experiments demonstrates how difficult it would have been to predict that seasonal anomaly. Prescribing observed SST/SIC anomalies does not suffice, which suggests that even perfectly predicting SST months in advance would not have been enough to predict the seasonal Rossby wave and associated precipitation. After prescribing perfect tropical variability through nudging (which imposes observed MJO and other tropical variability in the model), the response is still different from observations and only nudging Arctic variability as well allows for a more realistic response. Even though it is unclear how much predictability exists at the seasonal time scale in the high latitudes, this highlights the need to explore the role of high-latitude climate processes in driving midlatitude variability. Sea ice was prescribed in our experiments, but other drivers

such as Arctic tropospheric temperature and the stratospheric polar vortex may exhibit some predictability and exert an influence in midlatitudes (Singh et al. 2018). One caveat of any model experiment is that it may miss important processes responsible for SWUS precipitation (large-scale teleconnections as well as small-scale processes, for example, linked to orography), such that this estimate of potential predictability coming from SST, the tropics, and the Arctic is inaccurate and too low. However, we note that WACCM4 was able to accurately simulate the 1983 El Niño teleconnection and record-breaking CA precipitation, as well as the 2016 El Niño teleconnection and CA moderate precipitation after nudging the tropics (Peings et al. 2022). This makes us more confident that the difficulty in reproducing the 2017 seasonal anomaly does not simply come from model limitations but from the fact that it is a manifestation of internal atmospheric variability that is hardly predictable.

Overall, our study underscores how challenging it is to predict seasonal SWUS precipitation a few months in advance. It is possible that predictable signals are too limited to gain significant skill in the future, but our study also conveys a positive message in that the models may not be adequate yet for

predicting it and may exhibit greater skill with future improvements in their basic state and teleconnections. Advanced machine learning techniques also represent an avenue for improving long-term forecasting, not only because data-driven weather/climate forecast models develop quickly (Ebert-Uphoff and Hilburn 2023) but also because they represent a tool to understand dynamical model biases. For instance, Gibson et al. (2021) developed a suite of machine learning algorithms to predict western U.S. precipitation regimes, which they trained using the CESM1 large ensemble. This highlighted the overestimation of the influence of ENSO in CESM1, when it comes to drivers of western U.S. precipitation. A similar approach could be applied to S2S and seasonal hindcasts/forecasts to further evaluate what drives SWUS precipitation in the models versus observations. Possibly, post-processing corrections may then be applied to the forecasts to account for known model limitations in key drivers of SWUS precipitation. This is a prospect for future research. Finally, in this study, we evaluated the models based on the 6-month ONDJFM season, while the influence of ENSO in seasonal prediction is generally evaluated over 3-month seasons that are typically used for seasonal forecast outlooks (e.g., Deser et al. 2018). Although additional analyses not shown in this paper suggest our general conclusions also apply to 3-month averages, it will be interesting to revisit them in more detail for DJF or JFM when ENSO teleconnections are the strongest.

Data availability statement. The ERA5 and C3S data are available at https://cds.climate.copernicus.eu. The HadISST data are available at https://www.metoffice.gov.uk/hadobs/hadisst/. GPCP precipitation is available at https://climatedataguide.ucar.edu/climate-data/gpcp-monthly-global-precipitation-climatology-project. CPC precipitation is available at https://psl.noaa.gov/data/gridded/data.cpc.globalprecip.html.

REFERENCES

Adler, R. F., and Coauthors, 2018: The Global Precipitation Climatology Project (GPCP) monthly analysis (new version 2.3) and a review of 2017 global precipitation. *Atmosphere*, **9**, 138, https://doi.org/10.3390/atmos9040138.

Barnston, A. G., A. Leetmaa, V. E. Kousky, R. E. Livezey, E. A. O'Lenic, H. Van den Dool, A. J. Wagner, and D. A. Unger, 1999: NCEP forecasts of the El Niño of 1997–98 and its U.S. impacts. *Bull. Amer. Meteor. Soc.*, **80**, 1829–1852, https://doi.org/10.1175/1520-0477(1999)080<1829:NFOTEN>2.0.CO;2.

Batté, L., C. Dorel, C. Ardilouze, and J.-F. Guérémy, 2021: Documentation of the METEO-FRANCE seasonal forecasting system 8. Tech. Rep., 36 pp., http://www.umr-cnrm.fr/IMG/pdf/system8-technical.pdf.

Bayr, T., D. I. V. Domeisen, and C. Wengel, 2019: The effect of the equatorial Pacific cold SST bias on simulated ENSO teleconnections to the North Pacific and California. *Climate Dyn.*, **53**, 3771–3789, https://doi.org/10.1007/s00382-019-04746-9.

Becker, E. J., B. P. Kirtman, M. L'Heureux, Á. G. Muñoz, and K. Pegion, 2022: A decade of the North American Multimodel Ensemble (NMME): Research, application, and future directions. *Bull. Amer. Meteor. Soc.*, **103**, E973–E995, https://doi.org/10.1175/BAMS-D-20-0327.1.

Bellenger, H., E. Guilyardi, J. Leloup, M. Lengaigne, and J. Vialard, 2014: ENSO representation in climate models: From CMIP3 to CMIP5. *Climate Dyn.*, **42**, 1999–2018, https://doi.org/10.1007/s00382-013-1783-z.

Beverley, J. D., M. Newman, and A. Hoell, 2023: Rapid development of systematic ENSO-related seasonal forecast errors. *Geophys. Res. Lett.*, **50**, e2022GL102249, https://doi.org/10.1029/2022GL102249.

Branstator, G., and H. Teng, 2017: Tropospheric waveguide teleconnections and their seasonality. *J. Atmos. Sci.*, **74**, 1513–1532, https://doi.org/10.1175/JAS-D-16-0305.1.

Chen, M., and A. Kumar, 2018: Winter 2015/16 atmospheric and precipitation anomalies over North America: El Niño response and the role of noise. *Mon. Wea. Rev.*, **146**, 909–927, https://doi.org/10.1175/MWR-D-17-0116.1.

——, W. Shi, P. Xie, V. B. S. Silva, V. E. Kousky, R. Wayne Higgins, and J. E. Janowiak, 2008: Assessing objective techniques for gauge-based analyses of global daily precipitation. *J. Geophys. Res.*, **113**, D04110, https://doi.org/10.1029/2007JD009132.

DeFlorio, M. J., and Coauthors, 2024: From California's extreme drought to major flooding: Evaluating and synthesizing experimental seasonal and subseasonal forecasts of landfalling atmospheric rivers and extreme precipitation during Winter 2022/23. *Bull. Amer. Meteor. Soc.*, **105**, E84–E104, https://doi.org/10.1175/BAMS-D-22-0208.1.

Deser, C., I. R. Simpson, A. S. Phillips, and K. A. McKinnon, 2018: How well do we know ENSO's climate impacts over North America, and how do we evaluate models accordingly? *J. Climate*, **31**, 4991–5014, https://doi.org/10.1175/JCLI-D-17-0783.1.

Dettinger, M. D., 2013: Atmospheric rivers as drought busters on the U.S. West Coast. *J. Hydrometeor.*, **14**, 1721–1732, https://doi.org/10.1175/JHM-D-13-02.1.

Dias, J., S. N. Tulich, M. Gehne, and G. N. Kiladis, 2021: Tropical origins of weeks 2–4 forecast errors during the Northern Hemisphere cool season. *Mon. Wea. Rev.*, **149**, 2975–2991, https://doi.org/10.1175/MWR-D-21-0020.1.

Ding, H., M. Newman, M. A. Alexander, and A. T. Wittenberg, 2018: Skillful climate forecasts of the tropical Indo-Pacific Ocean using model-analogs. *J. Climate*, **31**, 5437–5459, https://doi.org/10.1175/JCLI-D-17-0661.1.

——, ——, ——, and ——, 2019: Diagnosing secular variations in retrospective ENSO seasonal forecast skill using CMIP5 model-analogs. *Geophys. Res. Lett.*, **46**, 1721–1730, https://doi.org/10.1029/2018GL080598.

——, ——, ——, ——, 2020: Relating CMIP5 model biases to seasonal forecast skill in the tropical Pacific. *Geophys. Res. Lett.*, **47**, e2019GL086765, https://doi.org/10.1029/2019GL086765.

Dong, C., Y. Peings, and G. Magnusdottir, 2023: Regulation of southwestern United States precipitation by non-ENSO teleconnections and the impact of the background flow. *J. Climate*, **36**, 7415–7433, https://doi.org/10.1175/JCLI-D-23-0081.1.

——, ——, and ——, 2024: How do forecast model biases affect large-scale teleconnections that control Southwest U.S. precipitation? Part I: S2S models. *J. Climate*, **37**, 5409–5426, https://doi.org/10.1175/JCLI-D-24-0051.1.

Ebert-Uphoff, I., and K. Hilburn, 2023: The outlook for AI weather prediction. *Nature*, **619**, 473–474, https://doi.org/10.1038/d41586-023-02084-9.

Fröhlich, K., and Coauthors, 2021: The German Climate Forecast System: GCFS. *J. Adv. Model. Earth Syst.*, **13**, e2020MS002101, https://doi.org/10.1029/2020MS002101.

Garfinkel, C. I., W. Chen, Y. Li, C. Schwartz, P. Yadav, and D. Domeisen, 2022: The winter North Pacific teleconnection in response to ENSO and the MJO in operational subseasonal forecasting models is too weak. *J. Climate*, **35**, 8013–8030, https://doi.org/10.1175/JCLI-D-22-0179.1.

Gelaro, R., and Coauthors, 2017: The Modern-Era Retrospective Analysis for Research and Applications, version 2 (MERRA-2). *J. Climate*, **30**, 5419–5454, https://doi.org/10.1175/JCLI-D-16-0758.1.

Gibson, P. B., D. E. Waliser, B. Guan, M. J. DeFlorio, F. M. Ralph, and D. L. Swain, 2020: Ridging associated with drought across the western and southwestern United States: Characteristics, trends, and predictability sources. *J. Climate*, **33**, 2485–2508, https://doi.org/10.1175/JCLI-D-19-0439.1.

——, W. E. Chapman, A. Altinok, L. Delle Monache, M. J. DeFlorio, and D. E. Waliser, 2021: Training machine learning models on climate model output yields skillful interpretable seasonal precipitation forecasts. *Commun. Earth Environ.*, **2**, 159, https://doi.org/10.1038/s43247-021-00225-4.

Gualdi, S., and Coauthors, 2020: The new CMCC operational seasonal prediction system. 34 pp., https://doi.org/10.25424/CMCC/SPS3.5.

Guirguis, K., A. Gershunov, T. Shulgina, R. E. S. Clemesha, and F. M. Ralph, 2019: Atmospheric rivers impacting Northern California and their modulation by a variable climate. *Climate Dyn.*, **52**, 6569–6583, https://doi.org/10.1007/s00382-018-4532-5.

Hersbach, H., and Coauthors, 2020: The ERA5 global reanalysis. *Quart. J. Roy. Meteor. Soc.*, **146**, 1999–2049, https://doi.org/10.1002/qj.3803.

Horel, J. D., and J. M. Wallace, 1981: Planetary-scale atmospheric phenomena associated with the Southern Oscillation. *Mon. Wea. Rev.*, **109**, 813–829, https://doi.org/10.1175/1520-0493(1981)109<0813:PSAPAW>2.0.CO;2.

Hoskins, B. J., and D. J. Karoly, 1981: The steady linear response of a spherical atmosphere to thermal and orographic forcing. *J. Atmos. Sci.*, **38**, 1179–1196, https://doi.org/10.1175/1520-0469(1981)038<1179:TSLROA>2.0.CO;2.

——, and T. Ambrizzi, 1993: Rossby wave propagation on a realistic longitudinally varying flow. *J. Atmos. Sci.*, **50**, 1661–1671, https://doi.org/10.1175/1520-0469(1993)050<1661:RWPOAR>2.0.CO;2.

Hurrell, J. W., J. J. Hack, D. Shea, J. M. Caron, and J. Rosinski, 2008: A new sea surface temperature and sea ice boundary dataset for the Community Atmosphere Model. *J. Climate*, **21**, 5145–5153, https://doi.org/10.1175/2008JCLI2292.1.

Jiang, X., D. E. Waliser, P. B. Gibson, G. Chen, and W. Guan, 2022: Why seasonal prediction of California winter precipitation is challenging. *Bull. Amer. Meteor. Soc.*, **103**, E2688–E2700, https://doi.org/10.1175/BAMS-D-21-0252.1.

Johnson, S. J., and Coauthors, 2019: SEAS5: The new ECMWF seasonal forecast system. *Geosci. Model Dev.*, **12**, 1087–1117, https://doi.org/10.5194/gmd-12-1087-2019.

Karanja, J., B. M. Svoma, J. Walter, and M. Georgescu, 2023: Southwest US winter precipitation variability: Reviewing the role of oceanic teleconnections. *Environ. Res. Lett.*, **18**, 053003, https://doi.org/10.1088/1748-9326/accd84.

Kay, J. E., and Coauthors, 2015: The Community Earth System Model (CESM) large ensemble project: A community resource for studying climate change in the presence of internal climate variability. *Bull. Amer. Meteor. Soc.*, **96**, 1333–1349, https://doi.org/10.1175/BAMS-D-13-00255.1.

Kumar, A., and M. Chen, 2017: What is the variability in US West Coast winter precipitation during strong El Niño events? *Climate Dyn.*, **49**, 2789–2802, https://doi.org/10.1007/s00382-016-3485-9.

——, and ——, 2020: Understanding skill of seasonal mean precipitation prediction over California during boreal winter and role of predictability limits. *J. Climate*, **33**, 6141–6163, https://doi.org/10.1175/JCLI-D-19-0275.1.

Lee, S.-K., H. Lopez, E.-S. Chung, P. DiNezio, S.-W. Yeh, and A. T. Wittenberg, 2018: On the fragile relationship between El Niño and California rainfall. *Geophys. Res. Lett.*, **45**, 907–915, https://doi.org/10.1002/2017GL076197.

L'Heureux, M. L., M. K. Tippett, and A. G. Barnston, 2015: Characterizing ENSO coupled variability and its impact on North American seasonal precipitation and temperature. *J. Climate*, **28**, 4231–4245, https://doi.org/10.1175/JCLI-D-14-00508.1.

Li, R. K., T. Woollings, C. O'Reilly, and A. A. Scaife, 2020: Effect of the North Pacific tropospheric waveguide on the fidelity of model El Niño teleconnections. *J. Climate*, **33**, 5223–5237, https://doi.org/10.1175/JCLI-D-19-0156.1.

Lin, H., and Coauthors, 2020: The Canadian Seasonal to Interannual Prediction System version 2 (CanSIPSv2). *Wea. Forecasting*, **35**, 1317–1343, https://doi.org/10.1175/WAF-D-19-0259.1.

Ma, H.-Y., and Coauthors, 2021: On the correspondence between seasonal forecast biases and long-term climate biases in sea surface temperature. *J. Climate*, **34**, 427–446, https://doi.org/10.1175/JCLI-D-20-0338.1.

MacLachlan, C., and Coauthors, 2015: Global Seasonal forecast system version 5 (GloSea5): A high-resolution seasonal forecast system. *Quart. J. Roy. Meteor. Soc.*, **141**, 1072–1084, https://doi.org/10.1002/qj.2396.

Mamalakis, A., J.-Y. Yu, J. T. Randerson, A. AghaKouchak, and E. Foufoula-Georgiou, 2018: A new interhemispheric teleconnection increases predictability of winter precipitation in southwestern US. *Nat. Commun.*, **9**, 2332, https://doi.org/10.1038/s41467-018-04722-7.

Marsh, D. R., M. J. Mills, D. E. Kinnison, J.-F. Lamarque, N. Calvo, and L. M. Polvani, 2013: Climate change from 1850 to 2005 simulated in CESM1(WACCM). *J. Climate*, **26**, 7372–7391, https://doi.org/10.1175/JCLI-D-12-00558.1.

Meinshausen, M., and Coauthors, 2011: The RCP greenhouse gas concentrations and their extensions from 1765 to 2300. *Climatic Change*, **109**, 213, https://doi.org/10.1007/s10584-011-0156-z.

Mundhenk, B. D., E. A. Barnes, E. D. Maloney, and K. M. Nardi, 2016: Modulation of atmospheric rivers near Alaska and the U.S. West Coast by northeast Pacific height anomalies. *J. Geophys. Res. Atmos.*, **121**, 12 751–12 765, https://doi.org/10.1002/2016JD025350.

Payne, A. E., and G. Magnusdottir, 2016: Persistent landfalling atmospheric rivers over the west coast of North America. *J. Geophys. Res. Atmos.*, **121**, 13 287–13 300, https://doi.org/10.1002/2016JD025549.

Peings, Y., Y. Lim, and G. Magnusdottir, 2022: Potential predictability of Southwest U.S. rainfall: Role of tropical and high-latitude variability. *J. Climate*, **35**, 1697–1717, https://doi.org/10.1175/JCLI-D-21-0775.1.

Ralph, F. M., and M. D. Dettinger, 2011: Storms, floods, and the science of atmospheric rivers. *Eos, Trans. Amer. Geophys. Union*, **92**, 265–266, https://doi.org/10.1029/2011EO320001.

Rayner, N. A., D. E. Parker, E. B. Horton, C. K. Folland, L. V. Alexander, D. P. Rowell, E. C. Kent, and A. Kaplan, 2003: Global analyses of sea surface temperature, sea ice, and night marine air temperature since the late nineteenth century. *J. Geophys. Res.*, **108**, 4407, https://doi.org/10.1029/2002JD002670.

Ropelewski, C. F., and M. S. Halpert, 1986: North American precipitation and temperature patterns associated with the El Niño/Southern Oscillation (ENSO). *Mon. Wea. Rev.*, **114**, 2352–2362, https://doi.org/10.1175/1520-0493(1986)114<2352:NAPATP>2.0.CO;2.

Roy, T., X. He, P. Lin, H. E. Beck, C. Castro, and E. F. Wood, 2020: Global evaluation of seasonal precipitation and temperature forecasts from NMME. *J. Hydrometeor.*, **21**, 2473–2486, https://doi.org/10.1175/JHM-D-19-0095.1.

Seager, R., and N. Henderson, 2016: On the role of tropical ocean forcing of the persistent North American west coast ridge of winter 2013/14. *J. Climate*, **29**, 8027–8049, https://doi.org/10.1175/JCLI-D-16-0145.1.

Sengupta, A., B. Singh, M. J. DeFlorio, C. Raymond, A. W. Robertson, X. Zeng, D. E. Waliser, and J. Jones, 2022: Advances in subseasonal to seasonal prediction relevant to water management in the western United States. *Bull. Amer. Meteor. Soc.*, **103**, E2168–E2175, https://doi.org/10.1175/BAMS-D-22-0146.1.

Singh, D., M. Ting, A. A. Scaife, and N. Martin, 2018: California winter precipitation predictability: Insights from the anomalous 2015–2016 and 2016–2017 seasons. *Geophys. Res. Lett.*, **45**, 9972–9980, https://doi.org/10.1029/2018GL078844.

Smith, K. L., R. R. Neely, D. R. Marsh, and L. M. Polvani, 2014: The Specified Chemistry Whole Atmosphere Community Climate Model (SC-WACCM), *J. Adv. Model. Earth Syst.*, **6**, 883–901, https://doi.org/10.1002/2014MS000346.

Sun, L., M. P. Hoerling, J. H. Richter, A. Hoell, A. Kumar, and J. W. Hurrell, 2022: Attribution of North American subseasonal precipitation prediction skill. *Wea. Forecasting*, **37**, 2069–2085, https://doi.org/10.1175/WAF-D-22-0076.1.

Swain, D. L., 2015: A tale of two California droughts: Lessons amidst record warmth and dryness in a region of complex physical and human geography. *Geophys. Res. Lett.*, **42**, 9999–10003, https://doi.org/10.1002/2015GL066628.

——, D. Singh, D. E. Horton, J. S. Mankin, T. C. Ballard, and N. S. Diffenbaugh, 2017: Remote linkages to anomalous winter atmospheric ridging over the northeastern Pacific. *J. Geophys. Res. Atmos.*, **122**, 12194–12209, https://doi.org/10.1002/2017JD026575.

Switanek, M. B., and T. M. Hamill, 2022: A new methodology to produce more skillful United States cool-season precipitation forecasts. *J. Hydrometeor.*, **23**, 991–1005, https://doi.org/10.1175/JHM-D-21-0235.1.

——, J. J. Barsugli, M. Scheuerer, and T. M. Hamill, 2020: Present and past sea surface temperatures: A recipe for better seasonal climate forecasts. *Wea. Forecasting*, **35**, 1221–1234, https://doi.org/10.1175/WAF-D-19-0241.1.

Teng, H., and G. Branstator, 2017: Causes of extreme ridges that induce California droughts. *J. Climate*, **30**, 1477–1492, https://doi.org/10.1175/JCLI-D-16-0524.1.

Trenberth, K. E., G. W. Branstator, D. Karoly, A. Kumar, N.-C. Lau, and C. Ropelewski, 1998: Progress during TOGA in understanding and modeling global teleconnections associated with tropical sea surface temperatures. *J. Geophys. Res.*, **103**, 14291–14324, https://doi.org/10.1029/97JC01444.

Wang, J., H. Kim, D. Kim, S. A. Henderson, C. Stan, and E. D. Maloney, 2020: MJO teleconnections over the PNA region in climate models. Part II: Impacts of the MJO and basic state. *J. Climate*, **33**, 5081–5101, https://doi.org/10.1175/JCLI-D-19-0865.1.

Wang, S.-Y. S., J.-H. Yoon, E. Becker, and R. Gillies, 2017: California from drought to deluge. *Nat. Climate Change*, **7**, 465–468, https://doi.org/10.1038/nclimate3330.

Williams, N. C., A. A. Scaife, and J. A. Screen, 2023: Underpredicted ENSO teleconnections in seasonal forecasts. *Geophys. Res. Lett.*, **50**, e2022GL101689, https://doi.org/10.1029/2022GL101689.

Yonehara, H., and Coauthors, 2020: Upgrade of JMA's operational global model. *CAS/JSC WGNE Res. Act. Earth Syst. Modell.*, **50**, 6.19–6.20.

Zhang, W., and G. Villarini, 2018: Uncovering the role of the East Asian jet stream and heterogeneities in atmospheric rivers affecting the western United States. *Proc. Natl. Acad. Sci. USA*, **115**, 891–896, https://doi.org/10.1073/pnas.1717883115.